SAND2020-10352

SANDIA REPORT
SAND20213047
Printed September 2020

Sandia National Laboratories

Mobile Cross-polarized NQR: Buried Explosive Detection from a Safe Distance

Eric Glenn Sorte

Prepared by
Sandia National Laboratories
Albuquerque, New Mexico
87185 and Livermore,
California 94550

Issued by Sandia National Laboratories, operated for the United States Department of Energy by National Technology & Engineering Solutions of Sandia, LLC.

Available to DOE and DOE contractors from
U.S. Department of Energy
Office of Scientific and Technical Information
P.O. Box 62
Oak Ridge, TN 37831

Telephone: (865) 576-8401
Facsimile: (865) 576-5728
E-Mail: reports@osti.gov
Online ordering: http://www.osti.gov/scitech

Available to the public from
U.S. Department of Commerce
National Technical Information Service
5301 Shawnee Rd
Alexandria, VA 22312

Telephone: (800) 553-6847
Facsimile: (703) 605-6900
E-Mail: orders@ntis.gov
Online order: https://classic.ntis.gov/help/order-methods/

ABSTRACT

Nuclear quadrupole resonance is a non-destructive detection and inspection technique with potential as a non-destructive test (NDT) tool. Establishment of the capability opens the door to its use in furthering the mission of the labs. There are many possible uses of the capability: explosive detection and stress/strain detection in epoxies are two of the more obvious and are the main results of this work. Enhancement of the signal-to-noise ratio (SNR) and improvements in the acquisition time of the experiment were key focuses of this work. These were achieved by combing special spin-lock pulse sequences with cross-polarization (CP) schemes to improve the signals with shorter acquisition times. A novel rotating magnetic field device was created to facilitate CP in the field. Implementation of these schemes provided a significant reduction in SNR/time.

ACKNOWLEDGEMENTS

Ehren Baca contributed significantly to this work, especially in the design, manufacture, and construction of the rotating magnetic arm. Brad Jones was instrumental in making and testing Cu_2O impregnated epoxies for the stress measurement effort. Jessica Rimsza and Nathan Torgrimson did the DFT, MD, and circuit modeling.

CONTENTS

LIST OF FIGURES

LIST OF TABLES

This page left blank

ACRONYMS AND DEFINITIONS

Abbreviation	Definition
NDT	Non-destructive test
NQR	Nuclear quadrupole resonance
NMR	Nuclear magnetic resonance
MRI	Magnetic resonance imaging
RF	Radio frequency electromagnetic radiation
SNR	Signal to noise ratio
CP	Cross polarization
AN	Ammonium nitrate
T_1	Longitudinal relaxation time
T_2	Transverse relaxation time
AC	Alternating current
DC	Direct current
RPM	Rotations per minute
DFT	Density functional theory
AIMD	*Ab initio* molecular dynamics
COD	Crystallography Open Database
PBE	Perdew, Burke, and Ernzerhof
GIPAW	Gauge Including Projector Augmented Waves
CTE	Coefficient of thermal expansion
LAC	Lightning arrestor connectors

1. REMOTE SENSING BY NQR

1.1. History

Nuclear Quadrupole Resonance (NQR) as a characterization technique has its beginnings around the time the first NMR signals were detected in the 1940s. As an explosive detector, much work was done by Al Garroway and Joel Miller and team at NRL from the 1980s to the 2000s.[1-4] Some of the NRL technology was subsequently licensed to a private company named Quantum Magnetics, Inc. Quantum Magnetics, a subsidiary of InVision Technologies, was active in the use of magnetic resonance for security applications from 1988 and developed NQR systems for airport security, narcotics detection, and landmine detection since the early 1990s.[5,6] Lowell Burnett led Quantum Magnetics in the landmine detection field for many years, and thereafter Pablo Prado. The company was eventually sold to General Electric's Security Division. Separately, Prof. V. S. Grechishkin at Kaliningrad University in Russia worked on remote NQR detection since the 1970s and NQR detection for landmines and small package inspection since the 1980s.[2]

More recently, Michele Espy and Michael Malone at Los Alamos National Labs have been developing shuttled systems for explosive detection.[7,8] Other groups working on related technologies include the Sauer group;[9-11] in one notable paper they used a Rb magnetometer to detect the NQR signals.[10]

Eiichi Fukushima and Armando De Los Santos made a successful dynamite detector for checked airline baggage on behalf of FAA, more than 30 years ago. Together with Al Garroway, they spent several days under a boarding area at DFW helping with the tests. They draped surrogate dynamite samples over many checked bags under a boarding gate, working fast to not delay loading the bags onto planes. According to Dr. Fukushima, the planes backed out of the gate area by reversing engine thrusts which meant they got blasted with the 100 °F+ air every time a plane left the gate. The final tests were successful in that if the explosive is not packed in a conductor (like aluminum foil), the detection rate for some reasonable amount of dynamite was something like 95% at a rate for the inspection to not delay flights.

A few years later, FAA "loaned" the device to whoever the agency is that checked for cocaine in flower boxes coming to Miami from South America. Those tests were even more successful than for dynamite. The physics for identifying dynamite is to use a pulse sequence to isolate long T_1 and short T_2 signals, done with a combination of solid echoes and Hahn echoes.

1.2. Landmine Problem

The United Nations estimates that over 80 million landmines are in place around the world, with more being placed all the time. These are placed for a variety of reasons, from stopping/diverting tanks to stopping military personnel or simply as a tool of fear and terrorism. Normal military operation requirements are normally to find a way through a minefield to achieve an objective that usually does not include finding and neutralizing all the mines. Unfortunately, once the land is returned to normal use, a humanitarian problem remains as the mines remain active. The ability to quickly find and safely remove mines is a cogent and immediate need.

1.3. Limitations of Conventional Detection Methods

The basic method of detection for both military and humanitarian mine detection is still the electromagnetic metal detector. Detection of a conventional metal-encased antitank mine buried 10 cm underground is simple with these metal detectors. Finding a low-metal antipersonnel mine, however, is much more challenging. In such mines, there may only be a 0.5g of metal (firing pin) in the entire device, which requires that the gain on the metal detector be increased. Unfortunately, there are many things in the soil that contain metal at these levels – nails, discarded garbage, screws, etc. The operator must then use some means of confirming which signals are the result of actual mines and which are false signals, and this is principally done by mechanical probing. The operator must delicately attempt to classify the buried object with a pointed stick. This is potentially extremely hazardous. In this sense it is easy to find a mine but separating them from the clutter is difficult and dangerous.

1.4. Why NQR?

What is required is a detection method that would be specific to the landmine. A unique signature detected from the explosive mixture itself would be an ideal way to separate the signal from the clutter. The vapor pressure of military explosives used in landmines is very low, and commercially produced mines have hermetically sealed energetics in polymer cases. While there is some indication that extremely sensitive vapor detectors could detect the plumes from a landmine,[12] such devices are not readily available. NQR, however, could provide a unique fingerprint of an explosive substance regardless of packaging.

Apart from obtaining a unique chemical signature from a mine, NQR has many other advantages over other detection techniques. It is a truly non-invasive detector, and no vapor or particulate capture is required. It is immediate, and independent repeat measurements are possible to verify a detection event. The system cannot be saturated by a mine signal, it can be made simple to use (one button operation), its low power RF pulses are harmless to humans, it requires no consumables, and it is comprised of rugged solid-state hardware.[6] All that is required of the material of interest is that it be a crystalline solid comprised of NQR active nuclei[13] (see Figure 1).

2. BASICS OF NQR

NQR is a magnetic resonance phenomenon related to nuclear magnetic resonance (NMR) and its medical application MRI. In NMR/MRI, a large static magnetic field (1-20 Tesla) is applied to the sample of interest. This large magnetic field orients the spins of the target nuclei in the sample to preferentially align in the direction of the field (the low energy state). This creates a population difference, with more of the nuclei in this low energy state than nuclei in the high energy state (pointing anti-parallel to the field). The magnetism created by the population difference can be observed by applying a resonant radio frequency (RF) pulse at the correct amplitude, duration, and direction to rotate the bulk magnetization vector away from the equilibrium position along the magnetic field. The RF pulse can be chosen in such a way so that the magnetization of the sample ends up at right angles to the magnetic field, whereupon it can precess freely in the static field at a characteristic frequency. The precessing magnetization creates a time-dependent flux that induces a voltage in the apparatus, which can be amplified and detected as the NMR signal. NMR has been studied and employed to great effect and success in a vast variety of experiments, from simple chemical identification to diffusion rate studies to kinetic studies and beyond.

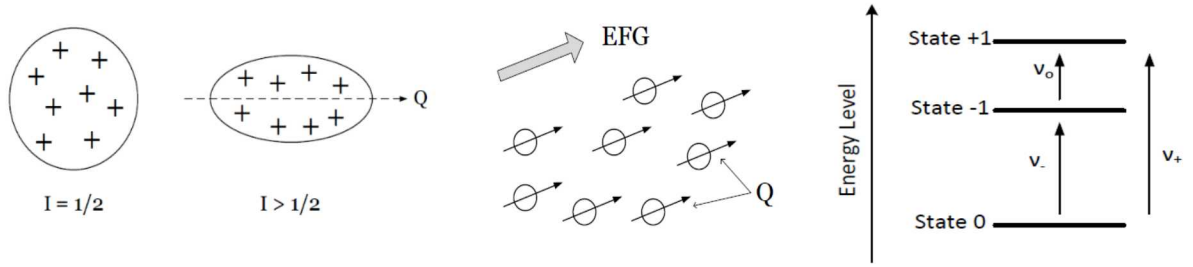

Figure 1. Left: nuclear charge density $\rho(r)$ for a spherical (I=1/2) charge distribution and an oblate (I>1/2) charge distribution with a quadrupole moment Q. Middle: Representation of the quadrupole moments Q of a sample align with the crystalline electric field gradients (EFGs). Right: Energy level diagram showing the nuclear energy level splitting induced by the interaction of the nuclear quadrupole moment with the lattice EFGs.

NQR is similar to NMR, but it has some important differences. In NQR, the nuclei similarly align, but not along a magnetic field. In fact, no magnetic field is required in an NQR experiment – this is one of the features that make it useful as a remote standoff detection capability. In NQR, the splitting of the nuclear spin states is accomplished by an electrostatic interaction between the nuclear charge density $\rho(r)$ with the external electric potential V(r) of the surrounding electron environment. A moment expansion of the interaction shows that the important coupling is between the nuclear quadrupole moment and the electric field gradient (EFG) or second derivative of V(r). The nuclear quadrupole moment Q is a parameter which describes the spatial distribution of the charge in the nucleus and is only non-zero for nuclei with spin quantum number ≥ 1. The electric potential V(r) is largely determined by the molecular structure surrounding the nucleus of interest, and is affected by the chemistry, crystal packing, and local electronic environment. All of this means that the signal observed in an NQR experiment will be determined not only by the nucleus of interest, but also by its particular chemical surroundings. In NMR, a hydrogen atom in an arbitrary chemical environment may experience a shift in frequency of around 10 parts per million around a central frequency chosen by the experimenter via the strength of the applied magnetic field. A ^{14}N nucleus in an NQR experiment could resonate anywhere between 0 - 6 MHz, and there is no "chosen frequency" that an

experimenter can chose as no magnetic field is applied. The increased sensitivity to chemical environment in an NQR experiment over an NMR experiment thus brings substantial benefit at substantial experimental cost in finding the resonance in the first place. Normally in NQR either the ν_- or ν_+ transitions are stimulated, and not the ν_0 transition (which arises from non-axial symmetry).[14]

Table 1 shows a table of some commonly used NQR-active nuclei along with their isotopic abundance, spin quantum number, gyromagnetic ratios and quadrupolar coupling constants.[13]

Table 1: Common quadrupolar nuclei

Nucleus	Natural Isotopic Abundance %	Spin I	$\gamma/2\pi$ (kHz/G)	Q (10^{-24} cm^2)
^{2}H	0.015	1	0.654	+0.00286
^{6}Li	7.4	1	0.626	–0.0008
^{7}Li	92.6	3/2	1.655	–0.040
^{10}B	19.6	3	0.458	+0.085
^{11}B	80.4	3/2	1.366	+0.041
^{14}N	99.6	1	0.308	+0.019
^{17}O	0.048	5/2	–0.577	–0.26
^{23}Na	100	3/2	1.126	+0.10
^{27}Al	100	5/2	1.109	+0.14
^{35}Cl	75.5	3/2	0.417	–0.082
^{37}Cl	24.5	3/2	0.347	–0.064
^{50}V	0.25	6	0.425	+0.21
^{51}V	99.8	7/2	1.119	–0.05
^{55}Mn	100	5/2	1.050	+0.33
^{59}Co	100	7/2	1.005	+0.40
^{63}Cu	69.1	3/2	1.128	–0.21
^{65}Cu	30.9	3/2	1.209	–0.195
^{69}Ga	60.4	3/2	1.022	+0.17
^{71}Ga	39.6	3/2	1.298	+0.10
^{75}As	100	3/2	0.729	+0.31
^{79}Br	50.5	3/2	1.067	+0.33
^{81}Br	49.5	3/2	1.150	+0.28
^{85}Rb	72	5/2	0.411	+0.23
^{87}Rb	28	3/2	1.393	+0.13
^{93}Nb	100	9/2	1.041	–0.32
^{113}In	4.3	9/2	0.931	+0.8
^{115}In	95.7	9/2	0.933	+0.8
^{121}Sb	57.3	5/2	1.019	–0.4
^{123}Sb	42.7	7/2	0.552	–0.5
^{127}I	100	5/2	0.852	–0.7
^{138}La	0.1	5	0.564	+0.4
^{139}La	99.9	7/2	0.606	+0.2
^{181}Ta	99.99	7/2	0.510	+3.3
^{197}Au	100	3/2	0.073	+0.55
^{209}Bi	100	9/2	0.684	–0.4
^{235}U	0.72	7/2	–0.076	+5

3. NQR HARDWARE AND SETUP

Our main NQR capability is centered around Tecmag spectrometers (LapNMR and Scout models). A schematic of the equipment setup is shown in Figure 2. The spectrometer receives instructions from the computer and outputs a low power RF pulse with the desired amplitude, phase, and duration to a 1 kW Tomco RF amplifier. That pulse is amplified to the desired amplitude and the high-power pulse is routed to a homebuilt transceiver/duplexer. The purpose of this module is to separate the transmit and receive pulses and to isolate the high power transmit pulse from the sensitive receive electronics. Lumped element filters stand in for quarter wave cables where physicals cables would be impractically long (at low frequencies). The transmit pulse is then coupled into a probe that is custom built for the specific application is mind. The probe normally consists of an inductor of custom shape for communicating the RF pulse to the sample as well as passive electronics to impedance match and make sure the probe absorbs energy at the right RF frequency with a high quality factor.

Once the transmit pulse is coupled into the inductor, the RF interacts with the sample as the corresponding nuclear response is induced. That response is coupled back into the same inductor as a tiny induced AC voltage. That voltage is then routed back to the duplexer, where it is amplified, filtered, and returned to the spectrometer for recording and analysis by the computer.

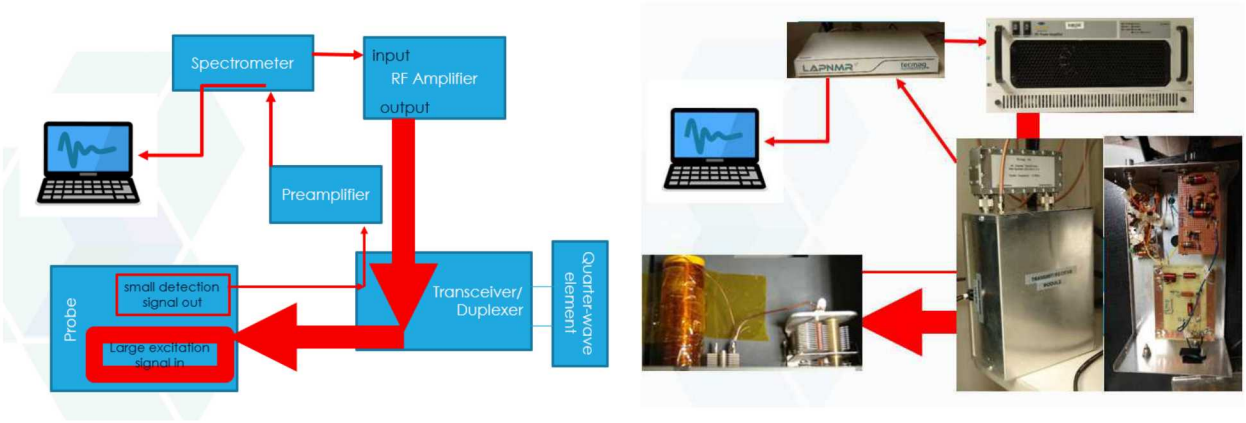

Figure 2. Left: block diagram view of the NQR spectrometer and associated modules. Right – physical implementation of the block diagram schematic.

Typical operating conditions for an enclosed solenoid coil such as the one pictured in Figure 2 are 50 microsecond pulses at a power of 250 W. Typical ringdown/dead time in the coil requires that data acquisition begin 20 microseconds after the final read pulse. Pulse sequences were typically repeated about 5x T_1 in short T_1 samples and somewhat faster for samples with long T_1s (one can calculate that about 0.75 x T_1 gives an optimal SNR/time for samples with long T_1). Signal averaging was done until adequate SNR was achieved.

Using wax-encased sodium nitrate (see Section 4.2), we verified a temperature dependence of 2.0 kHz/C, which agreed reasonably with that measured by Kim et al and others.[7,15] Relaxation times were measured to be $T_1 = 85\pm5$ ms and $T_2 = 4.3\pm0.2$ ms, which again agree with the literature.[7,16] Based on these measurements, we concluded that our NQR setup was functioning well and ready for use.

3.1. NQR as a remote detector

The main advantage provided by NQR is that it yields a highly specific (arguably unique) spectral fingerprint or frequency signature for the material of interest. For the over 10,000 compounds measured by NQR, no two have been found to be identical. Furthermore, only the compound of interest contributes to the signal, as the exact molecular structure around the nucleus is necessary to quantize the spins at the frequency of interest. NMR, in contrast, yields signals which are often highly convoluted, as ALL protons in and around a sample can contribute to the signal, and not just those of the material of interest. Figure 3 shows the NQR frequency fingerprints for several illicit substances and explosives. To avoid the difficulties of working with actual explosives, we chose proxies for two of the most important. These surrogates were chosen for their similar relaxation properties and excitation frequencies.

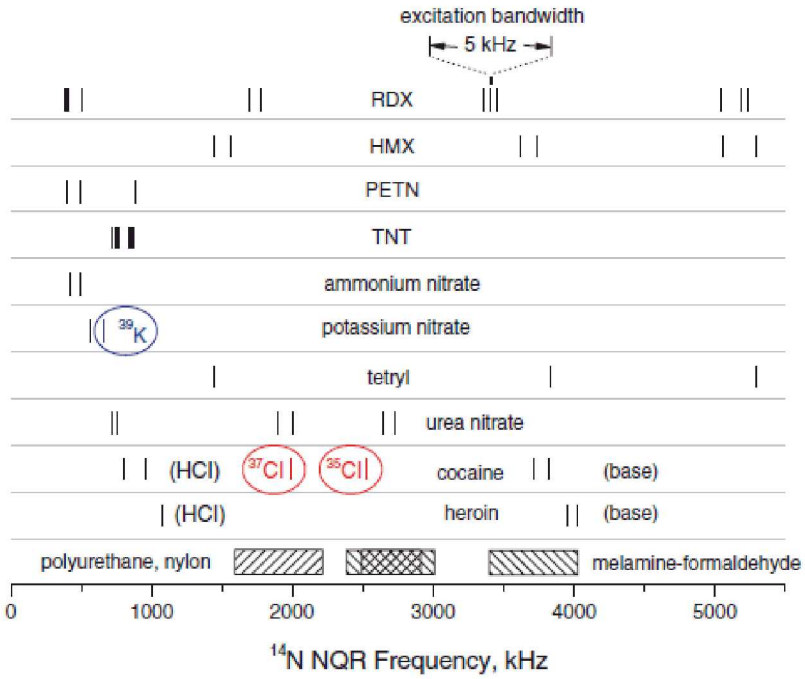

Figure 3: NQR frequencies of several illicit substances.

For landmine detection, RDX and TNT are the most important explosives. The explosives which can be easily detected by NQR include RDX ($C_3H_6N_6O_6$), HMX ($C_4H_8N_8O_8$), tetryl ($C_7H_5N_5O_8$), and their mixtures. However, explosives such as trinitrotoluene (TNT, $C_7H_5N_3O_6$), ammonium nitrate (AN), pentaerythritol tetranitrate PETN ($C_5H_8N_5O_{12}$) have much smaller signal-to-noise ratios because of lower NQR frequencies.

Several groups, including the NIST group, have made prototype mobile landmine detectors using NQR. One Japanese group in particular, lead by Professor Itozaki, even mounted their system to a remote controlled ATV;[17] see Figure 4. With their device, they were able to detect 100g of RDX buried at a depth of 15 cm in 2 seconds, and a similar amount of TNT at 5 cm depth in 15 min.

Figure 4: Mobile robotic ATV-mounted NQR detection system. Adapted from Ref 15.

For the purposes of this LDRD, proxies were identified to avoid the use of actual explosive chemicals in proof-of-concept experiments. For a proxy chemical to be instructive, it needs to have similar longitudinal (T_1) and transverse (T_2) relaxation times as well as a similar excitation frequency to the compound of interest.

3.2. Sodium Nitrite – A proxy for RDX

RDX has a T_1 of 10 ms, T_2 of 0.6 ms and a detection frequency around 3.6 MHz. For this we chose sodium nitrite ($NaNO_2$) as a proxy. Sodium nitrite has a T_1 = 50 ms, T_2 = 0.5 ms, and an excitation frequency at 3.6 MHz.

Figure 5 shows typical time and frequency domain signals of $NaNO_2$ acquired in 60 seconds with an SNR over 100 in a solenoid coil.

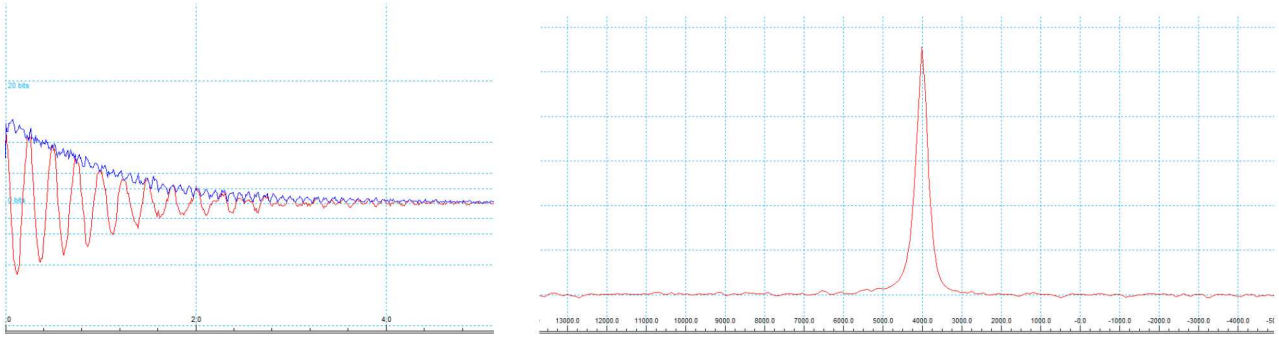

Figure 5 Left: Red line shows the quadrature NQR signal from 50 g of $NaNO_2$ in a solenoid coil. Blue line is the magnitude signal. Right: Fourier transform of the time domain signal.

Remote detection, of course, requires a stand-off means of detection for situations where it is impossible to encase the sample in a solenoid (such as buried explosives). To that end, we built a surface coil shown in Figure 6. Such coils have an approximate sensitivity equal to about one coil radius.[2] For detection 10 cm deep, we constructed the inner coil radius to be 10 cm. Matching and tuning electronics are located next to the coil in a shielded box, and a counter coil was counter wound above the first coil for noise mitigation. This coil was built to be rested on the ground over the area in question while the measurement is performed.

Figure 6: Surface coil for NQR measurements of buried samples.

Using the surface coil shown in Figure 6, we measured the SNR for an $NaNO_2$ sample buried to various depths. Using a 15 second acquisition experiment, a 50 g sample of wax-encased $NaNO_2$ placed directly inside the coil yielded a SNR of ~20. The sample was then moved below the detection coil to various depths, and the results are shown in Figure 7.

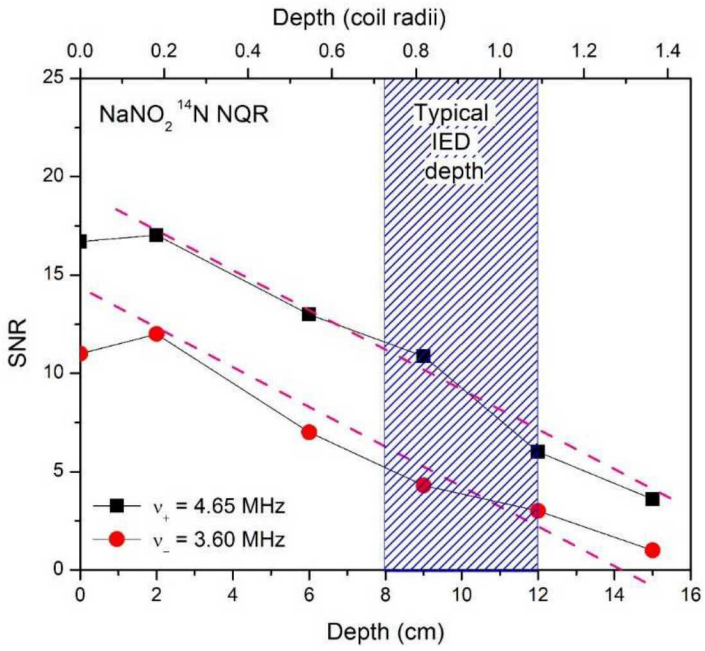

Figure 7: ^{14}N NQR. SNR as function of depth for $NaNO_2$. Both the ν_+ and ν_- transitions are shown.

In Figure 7, the blue hatched region highlights the region between 8 cm and 10 cm in depth, which corresponds to a typical anti-personnel mine burial depth. Using this detection protocol (15 sec acquisition), we can reliably achieve reliable detections using either nuclear transition of $NaNO_2$ at 3.6 MHz or 4.65 MHz, with the higher frequency more sensitive. The 3.6 MHz frequency is closest to RDX, however, and we show there that we can detect the RDX surrogate at 10 cm of depth with an SNR of 5 in about 15 seconds.

3.3. Ammonium Nitrate – A proxy for TNT

TNT has a T_1 of 6 sec, T_2 of 1.2 ms and a detection frequency around 0.85 MHz. For this compound, we chose ammonium nitrate AN (NH_4NO_3) as a proxy. AN has a T_1 = 10s, T_2 = 1.5 ms, and an excitation frequency at 0.424 MHz – and as an added bonus has some mission relevance itself due to the fact that it is a component in some explosives itself. Figure 8 shows typical time and frequency domain signals of AN acquired in about 1 hour with an SNR around 10 in a solenoid coil.

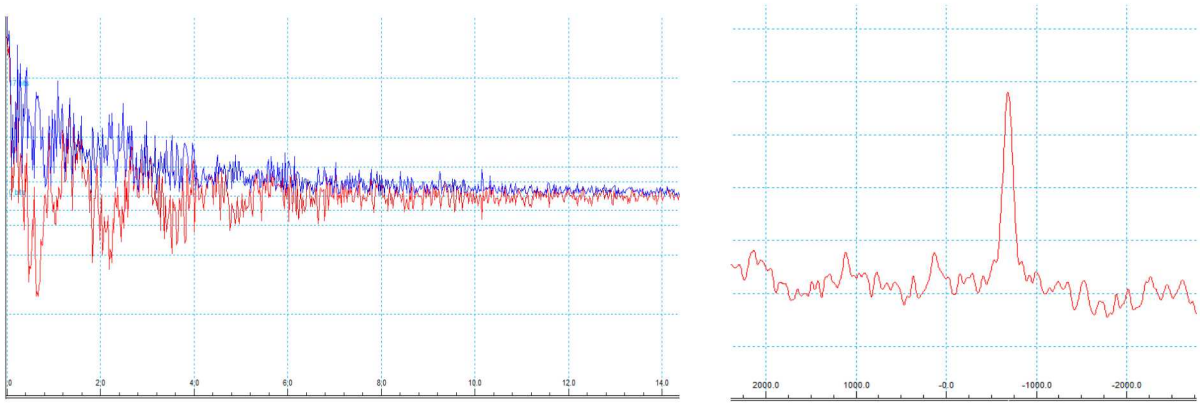

Figure 8 Left: Red line show the quadrature NQR signal from 50g of AN in a solenoid coil. Blue line is the magnitude signal. Right: Fourier transform of the time domain signal.

The AN compound has two NQR transition frequencies ν_+=496 kHz and ν_-=424 kHz (see Figure 1 and the surrounding discussion) both associated with the NO_3 ion. These transitions were first identified by the Blinc group.[18] We chose to work with the ν_-=424 kHz transition because it is less sensitive to temperature changes than the ν_+ transition.[19] AN has a melting point around 169 C; below that it exists in 5 different crystallographic polymorphs.[18] The stable form at room temperature has a phase transition to another form at only 32 C.[19]

We note the difference in performance between the sodium nitrite and ammonium nitrate examples shown here. For the sodium nitrite, SNR of 10 is achievable in just a few seconds. For AN, SNR of 10 takes over an hour to achieve. The relatively poor performance of the AN NQR is due to the low (< 1 MHz) excitation frequency and slow relaxation parameter T_1 which prohibits rapid signal averaging. This motivates the remainder of this report which is focused on improving that situation through signal enhancement mechanisms.

3.4. Known limitations, challenges and potential for improvement

The above section details our efforts in setting up a conventional NQR system, building custom probes, and recording signals on explosive material surrogates with similar excitation and relaxation properties to their explosive counterparts.

When designing and building an NQR system, several limitations and challenges should be kept in mind. First, NQR signals are notoriously temperature sensitive, so it is important to calibrate the frequency vs temperature curve for a given sample. The narrow bandwidth of a traditional probe and low pass filter will make a small window and you need to know the frequency well in order to avoid missing the detection. Second, an unoriented powder results in a 0.43 reduction in signal strength.[2] Furthermore, as shown by Garroway,[2] calculations shows that a typical landmine signal might come in around 20 nVpp (144 dBm), which is comparable to thermal noise at 28 nV (-138 dBm). Clearly noise reduction and signal optimization are going to be important design considerations.

Since this is a standoff measurement with a buried sample, antenna design is going to play another major role in the system's efficacy. A transmit and receive system is required that can project the RF excitation field to the appropriate depth and then detect the resulting NQR response signal, often in the 10's of nV regime. The antenna must operate over various ground materials and be able to withstand and mitigate a noisy RF environment.

Furthermore, the system must be able to detect TNT if it is to be of use. TNT is the most common explosive used in landmines, and unfortunately it is much more difficult to detect than other high explosives because the energy of its NQR response is divided among 12 spectral lines. High speed RF switching techniques to enable multiline detection are would make detection easier. It has been noted, however, in investigations of the relative effect of the ground that the incremental improvement of complex coil designs does not justify the resulting increase in antenna weight. cost, and power dissipation.[20]

4. ENHANCING THE SNR

The difficulties of detecting compounds with low frequency transitions and slow relaxation times outlined above make the necessity of enhancing the acquisition in some way important. There are several tracks one can take to enhance the SNR in such situations. Properly designing the detection coil and the supporting electronics can go a long way to minimizing noise in the acquisitions. Simulations to understand and optimize the probe circuitry will be important to understand the noise limits of the probe.

Beyond optimizing the hardware, there are several more exotic enhancement techniques that can be employed. The use of multi-pulse spin locking sequences have been found to improve SNR in a single acquisition by co-adding multiple echoes from a train.[21] Additionally, if the sample's ^{14}N nuclei have ^{1}H nuclei in close proximity (1-2 bond lengths away), cross-polarization schemes borrowed from solid state NMR can move magnetization from the protons to the ^{14}N, enhancing the magnetization of the ^{14}N while at the same time reducing the time needed between signal acquisitions. Finally, clever strategies to minimize the radio frequency interference (RFI) in the signal will help reduce the noise floor even further.

4.1. Coil design and electronics

For lab-based NQR studies, building a shielded solenoid inductor with high breakdown voltage capacitors is the optimal low noise detector. Figure 9 shows an example probe (lid removed) with a solenoid inductor and air-variable capacitors used in our lab. The inductor was built to receive a 50g centrifuge tube containing the sample. Such probes can be built with wide tuning/matching ranges to accommodate a range of samples.

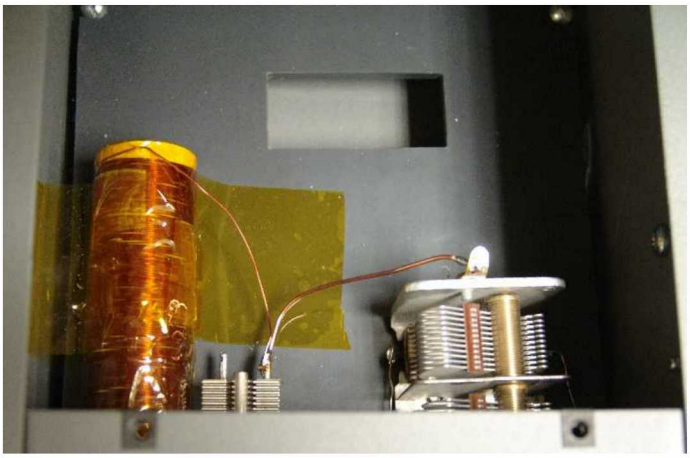

Figure 9: Example of a custom NQR probe built for $NaNO_2$ (2-5 MHz tuning range).

For remote detection, the superiority of a flat spiral over a solenoid design has already been shown by Rudakov et al.[19] in the case of a pair of identical planar surface coils with the sample placed between the two coils. Obviously such configuration is applicable for explosive detection, and it is the design we followed in our surface coil (see Section 3.2).[14]

4.2. Simulations

To understand the noise characteristics of the probe shown in Figure 9, we performed simulations in the QUCS software. The noise simulations were intended to understand the Johnson-Nyquist (thermal) noise. To do that, the simulation first calculates the noise density in the resistance of the inductor. Next, the noise power delivered to a 50 Ω load through the capacitive divider was determined. The 50 Ω load represents the downstream electronics (including the preamp which has its own noise figure) and will set the noise floor of the entire system. The noise sources should add incoherently, and the largest (if more than ~5 dB different) will generally be the dominant source. Knowledge of which source of noise is dominant and its level will allow us to determine the minimum induced voltage (or minimum magnetic field) in the coil that will produce the same noise voltage and will determine the sensitivity of the probe. This will tell us the minimum signal strength we will need in order to observe it over the noise.

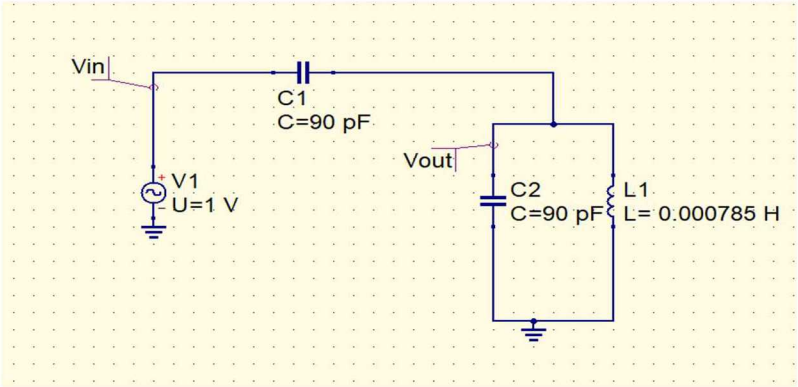

Figure 10: Schematic of the probe modeled as an ideal tank circuit using the capacitor and inductor values from the physical probe. Both capacitors are set to 90 pF, and the inductor is wound with 785 µH.

Figure 10 shows the probe tank circuit designed for AN. The resonating frequency for this circuit is given by

$$f = \frac{1}{2 * \pi} * \frac{1}{\sqrt{LC}}$$

This circuit has been tuned to resonate at *f*=424.7 kHz with *C1*=*C2*=90 pF and *L*=785 µH. The internal resistance of the inductor was measured at 424.7 kHz to be R=10 Ohms. This non-ideal model is show in Figure 11.

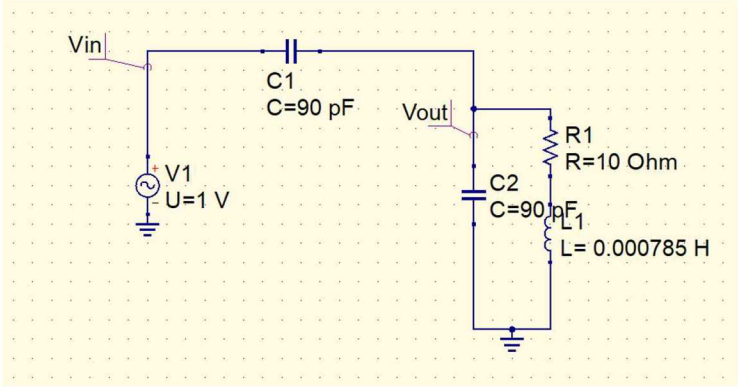

Figure 11: Non-ideal circuit with the addition of the inductor's resistance.

It is important to note that the inclusion of the internal resistance of the inductor does not significantly alter the resonant properties of the circuit. To show this, we modeled the resonant response of both the ideal tank circuit shown in Figure 10 and compared it to the non-ideal circuit in Figure 11; the result is shown in Figure 1Figure 12.

Ideal tank circuit (Figure 10)

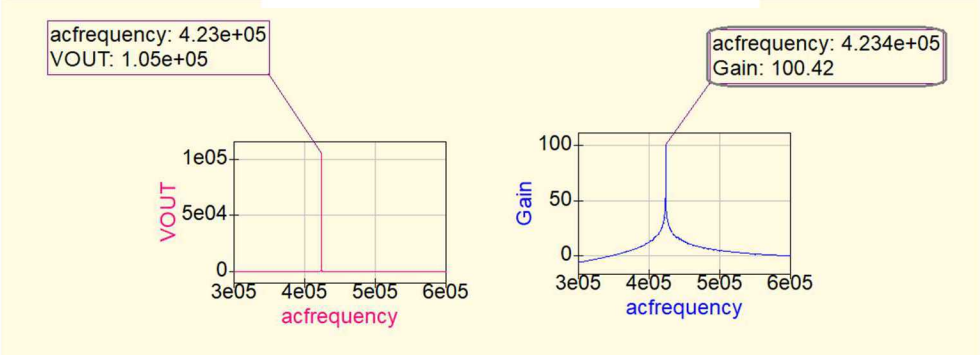

Non-ideal tank circuit (Figure 11)

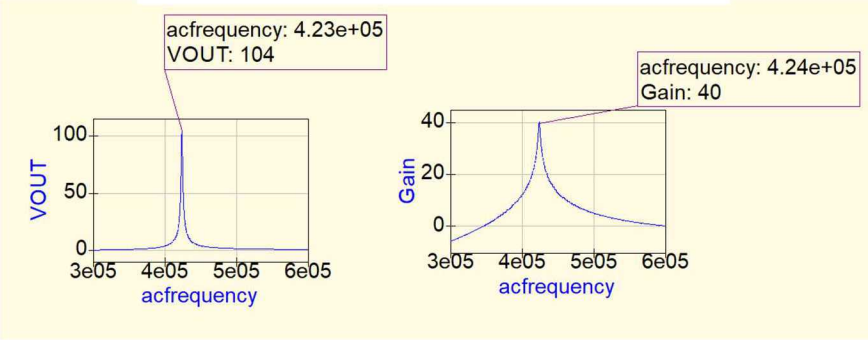

Figure 12: Gain and voltage characteristics of ideal (top) and non-ideal (bottom) circuits in Figures 10 and 11 respectively.

As shown in Figure 12, the addition of the lossy inductor doesn't change the resonant frequency but does initiate a quality factor Q which can be described by

$$Q = \frac{f}{\Delta f}$$

where f is the resonant frequency and Δf is the 3dB bandwidth of the probe. Q can be thought of as a dampening effect caused by the inductor's resistance. Also, note that the gain of the system has dropped drastically from 100 dB to 40 dB upon introduction of the internal inductor resistance. This is again caused by the energy not being focused at the resonant frequency and bleeding out to nearby frequencies.

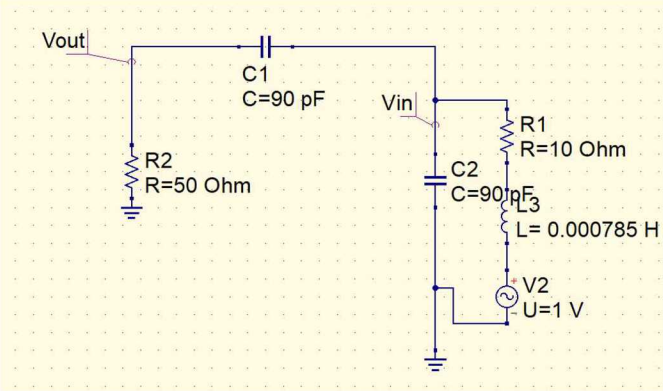

Figure 13: 50 Ω load driven by induced Voltage

Figure 13 is a close representation of how the probe functions. The sample nuclei's precession in the inductor will induce a voltage at the resonant frequency due to the precessing magnetization of the spin. That induced voltage will induce a current through the 50 Ω load (spectrometer) which will be then analyzed by the computer. The 50 Ω load also further dampens the system reducing the gain of the resonant circuit.

In order to determine the noise floor of the probe, the thermal noise of the system must be determined. The formula for thermal noise is given by

$$N = k * T * B,$$

where N is noise power in watts, T is temperature in Kelvin, k is the Boltzmann constant, and B is bandwidth of the system. For this case it is more useful to use the equation for power spectral density:

$$V = \sqrt{4k * T * R * B}\ ,$$

where R is resistance. There are only 2 sources of Nyquist noise in the system: 50 Ω load and the 10 Ω internal resistance of the inductor.

The power spectral density will be larger in the 50 Ω load than 10 Ω load as the only difference is the value of the resistance. The noise floor of the system is then

$$V_{noise} = \sqrt{4k * 300 * 50 * 10000}$$

$$=8.105*10^{-8}$$

which sets the noise floor of our system and determines the minimum detectable signal. So long as the induced voltage through the inductor is twice that of V_{noise} the signal will be detectable by this probe at the 50 Ω load with an SNR of 2.

4.3. Pulse sequence signal enhancement

Multi-pulse sequences borrowed from NMR[22-24] that can enhance an NQR signal have been studied and demonstrated by Rudakov and others.[3,21,25] There are many variations on the theme, but all involve spin-locking sequences derived from those proposed by Ostroff and Waugh[22]

$$\theta^0_{90^\circ} - \left(\tau - \theta^1_{0^\circ} - \tau -\right)_N,$$

where the second pulse θ^1 is phase shifted from the initial preparatory pulse θ^0 by 90° and τ is the time interval between the pulses. This sequence results in a refocusing of the transverse magnetization for periods much longer than T_2. It was first demonstrated in NQR by Klainer.[21] We used a variant demonstrated by Rudakov[25] called the spin-locking multi-pulse (SLMP) sequence:

$$\theta^0_{\varphi^\circ} - \left(\tau - \theta^1_{0^\circ} - 2\tau - \theta^1_{90^\circ} - 2\tau - \theta^1_{180^\circ} - 2\tau - \theta^1_{270^\circ} - \tau\right)_N$$

A simulation of the resulting echo stream is shown in Figure 14. The idea of these pulse sequences is that the persistent echo train contains multiple echoes *in one acquisition* that are identical apart from their reduction in intensity as a function of time. Therefore, if one co-adds the echoes in a train into one echo, a gain in SNR will be realized.

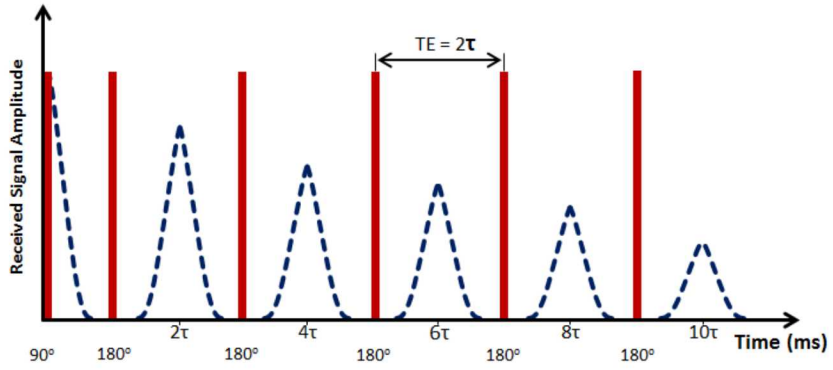

Figure 14: The SLMP echo sequence theoretical result.

Figure 15 shows our results using the SLMP pulse sequence on $NaNO_2$. In Figure 15a, a normal Hahn echo acquisition is shown. In Figure 15b, the result of the SLMP pulse sequence is shown. As is clear from the plots, persistent echoes are still forming after 60 ms, whereas the single echo has died

out around 30 ms. This demonstrates the fact that the transverse magnetization is indeed persisting well after the T_2 relaxation time of the compound. In Figure 15c and 15d, we can see the frequency domain signals associated with the single echo and the co-added echo train respectively on comparable intensity scales. For the same acquisition time, the SLMP pulse sequence yields a signal which is a factor of 3 higher in SNR that the single echo alone.

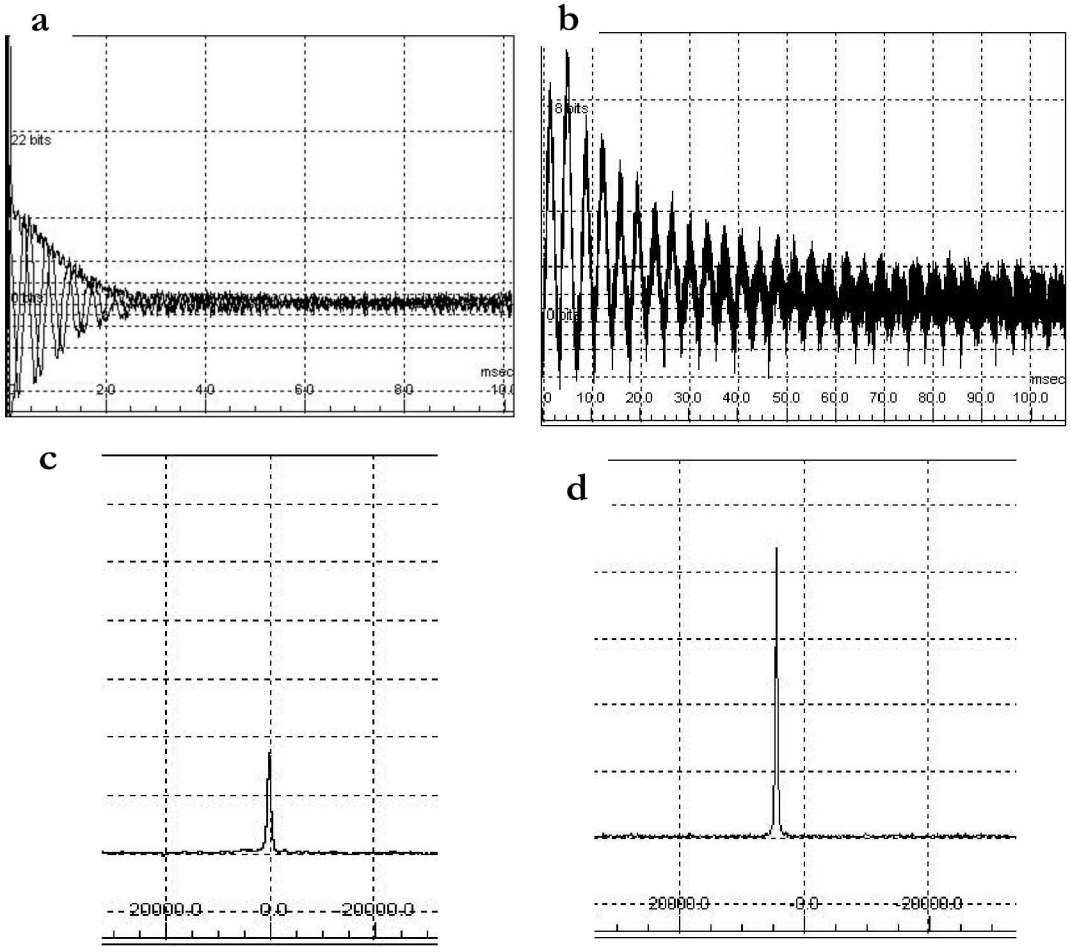

Figure 15: $NaNO_2$ NQR. a) Hahn echo acquisition with 32 averages repeated at 30 ms for a total of 1 second acquisition time. b) SLMP pulse sequence acquired with the same parameters, yielding an increase in SNR of a factor of 3 for the same acquisition time.

4.4. Cross-polarization signal enhancement

As early as the 1980s, researchers have been exploring the use of double resonance methods for NQR.[2,7,21,25,26] The approach uses a hybrid NMR/NQR approach in which a quasi-static magnetic field is rapidly ramped up and down. At high fields, a nuclear species with a large magnetic moment (such as protons) are magnetized to a maximum amount. As the field is lowered, the Zeeman splitting of the protons and the NQR splitting of the low magnetic moment species of interest (often ^{14}N) are brought into thermal contact, allowing the large magnetization of the protons to be exchanged with

the ^{14}N. This has been challenging to implement outside the laboratory, however, due to the difficulty in generating the required magnetic fields at depth.[2] In the laboratory, groups such as the Espy group at LANL have achieved polarization enhancements of a factor of 10 or more by shuttling a sample rapidly between a permanent magnet and NQR coil,[7,27] while others use swept voltage controlled fields to achieve the quasi-static magnetic environments.[11]

To understand how cross-polarization works for the NQR signal enhancement, consider Figure 16 which shows a nitrogen nucleus surrounded by proton nuclei. Initially, no magnetic field is present (left panel). In this environment, there is no net magnetization of the proton nuclei; their Zeeman splitting is absent with no magnetic field and both (equally populated) spin states have the same energy. The ^{14}N NQR transition is already resolved due to the EFG splitting, and thus there is a small net magnetization indicated by the small blue arrow. The energy level schematic next to the ion indicates the energy splitting in zero field. In the center panel, a large polarizing magnetic field is applied to the sample for a time long compared to the proton T_1. This splits the Zeeman levels of the proton and polarizes the proton magnetic moment by causing a population imbalance (more protons are in the low-energy state than the high energy state). The energy splitting of the proton is now much larger than the ^{14}N transition. The final step then is to bring the magnetic field down so that the proton energy level splitting matches that of the ^{14}N – the mixing field. This allows the two spin baths to exchange energy, polarizing the ^{14}N spins and enhancing the resulting signal. The cycle is then repeated for the next acquisition.

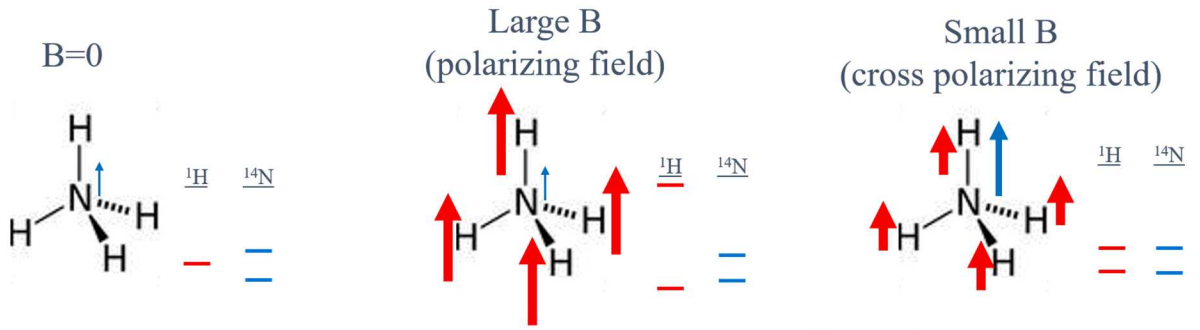

Figure 16: Cartoon illustrating the concept of cross polarization. Left: A ^{14}N and ^{1}H containing ion in zero magnetic field. The energy level diagram reflects the ^{14}N splitting due to the quadrupole moment interacting with the electric field gradients present in the lattice, while the Zeeman degeneracy of the ^{1}H is not lifted. Center: A large magnetic field is applied to the sample, splitting the Zeeman levels of the ^{1}H and polarizing the protons to a high level. Right: The magnetic field is adjusted to an appropriate mixing field value, where the ^{1}H Zeeman energy splitting and the ^{14}N NQR transition have the same value, allowing energy to flow from one spin bath to the other.

Note that in this scheme, it is the ^{1}H T_1 value that is the timescale of interest. This provides another mechanism for enhancement of SNR/time, since the ^{1}H T_1 is often much quicker than the slowly relaxing ^{14}N, allowing acquisitions to be repeated much more quickly. Further, the cross-polarization itself provides an additional relaxation path for the ^{1}H nuclei, so that the T_1 is reduced below what it would be normally.

4.4.1. Solenoid

To implement the cross polarization scheme in the lab, a solenoid magnet was built by ABQMR, LLC for the purpose. 1150 turn, 610 feet of #16 AWG magnet wire were used to build the coil on a steel frame. The resistance of the magnet was 2.6 Ω at room temperature.

At I=15 A and V=39 V, the power dissipated in the solenoid is P=585 W. Clearly, we would not want to run the magnet continuously at this power. By a calculation approximating the solenoid as infinite, the magnetic field generated is B=1422 Gauss, or 6.05 MHz for ^{1}H NMR. By measurement, R=2.35 Ω at 100 Hz; at higher frequencies R will increase due to eddy current loss in the coil support. With a Hall probe, we measured 412 Gauss at 4.91 A, so by linearity we expect B=419.5 Gauss at 5 amps and B=1259 Gauss at 15 Amps.

The electromagnet was set up in the lab with an isolation transformer and variable voltage source to dial in the voltage across the coil. Further, an isolation diode was put in parallel across the coil in order to avoid a large back voltage when breaking the circuit. The diode of course only functions at DC RF, not at AC. At 60 Hz, the magnet profile would look like that in Figure 17 (positive or negative polarization doesn't matter).

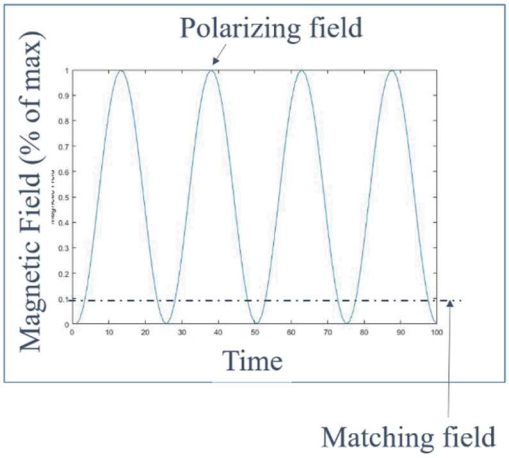

Figure 17: Magnet profile as a function of time for an AC excitation current.

This electromagnet proved useful for lab studies, but care had to be taken to keep it from heating and thereby heating the sample. NQR frequency transitions are highly temperature sensitive, and variations of only a few degrees can move the frequency of interest outside the sensitive bandwidth of the probe.

Consideration was next made about how to provide for a time-varying magnetic field at a standoff distance of 10 cm. The obvious choice is an electromagnet much like the coil made for the laboratory. Figure 18 shows some of our analysis on that point. In order to provide for a magnetic field of around 1000 Gauss (our target) with an electromagnet, we are looking at a 450 lbs electromagnet at relatively high cost (see left panel of Figure 18). The right panel of Figure 18 shows the corresponding size and weight of a permanent magnet. If a permanent magnet could be made to provide a time-varying field and not be extremely dangerous to handle, it would be two orders of magnitude lighter and cheaper.

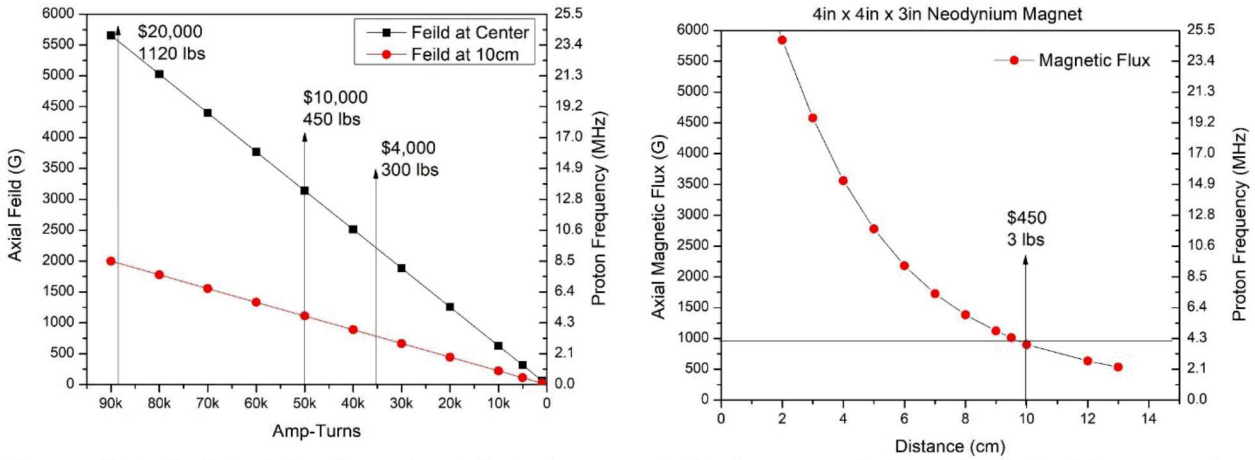

Figure 18: Left: Calculation for a standoff electromagnet. Black squares indicate the field at the magnet center, and the red circles corresponding field 10 cm below or above the coil windings. Right: Magnetic field values for a neodymium permanent magnet for comparison.

4.4.2. Spinning Magnets

One way to accomplish this would be to mount permanent magnets on a rotating state and spin them above the sample. To mitigate the safety concerns, one could use various commercial permanent magnets that can be "turned off". These ingenious arrangements stack two disk magnets within a flux-containing case, and a handle is mechanically attached to the top magnet to allow it to be rotated with respect to the bottom magnet. When the handle is turned such that the poles of the two magnets coincide (both north poles on the left, for example), the magnetic field is present at the bottom of the device, while the flux-containing case reduces the field at all other sides to near zero. When the top magnet is rotated such that the poles of the top magnet are opposite those of the bottom magnet, the fields effectively cancel, and no field is present even at the bottom.

Of course, the limiting value of the application of field cycling is the magnitude of the proton T_1. If T_1 shorter than the field cycling time, the technique will not work. T_1 if often field dependent as well; an additional item to keep under consideration.[28] It should be noted that the value of the cross-relaxation rate is much faster than the rates of longitudinal spin relaxation for either spin population independently. For AN, the cross-relaxation adds an additional relaxation path for both nuclear species. Best estimates of the proton T_1 are a few seconds at low fields.[29]

4.4.2.1. In the lab

The first implementation of the spinning magnet stage concept was performed in the lab at small scale. Four small magnets of around 1000 Gauss each were built and mounted on a stirring apparatus capable of 1000 RPM as shown in Figure 19.

Figure 19: Lab-scale rotating magnet stage for cross-polarization.

From the point of view of an AN molecule, a magnet will start directly overhead, subjecting the ^{1}H nuclei to the full strength of the magnetic field at the sample location. As the magnet moves, the field will rapidly decrease and then increase again as the next magnet moves into position. Since the ^{1}H T_1 is several seconds long, the decrease in field for millisecond timescales will not affect the polarization – it will continue to build until it reaches its full value at max field. The decrease in field will, however, reduce the Zeeman splitting of the ^{1}H nuclei to bring them into thermal contact with the ^{14}N NQR transition, allowing some of the proton magnetization to transfer to the weaker ^{14}N magnetization bath. As this process is repeated many times as the magnet stage rotates, it will act as a pump to move magnetization from the ^{1}H to the ^{14}N nuclei.

4.4.2.2. In the field

In order to mobilize the spinning magnet stage concept, a large prototype unit was built on the same principle but using larger magnets in order to project a significant field at depth (see Figure 20).

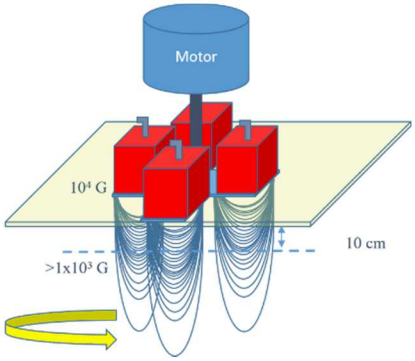

Figure 20: Schematic of the variable-field spinning magnet concept. Four 1-Tesla magnets are mounted and rotated at up to 900 rpm with a variable drive motor.

For the mobile unit, four 1-Tesla permanent magnets (with turn off capability) were mounted to a robust rotating stage with a variable drive motor. The magnets and drive shaft were mounted on a unistrut frame with the motor well-removed from the measurement area to reduce mechanical noise. Figure 21 show the magnet stage in several stages of assembly and the final assembled prototype.

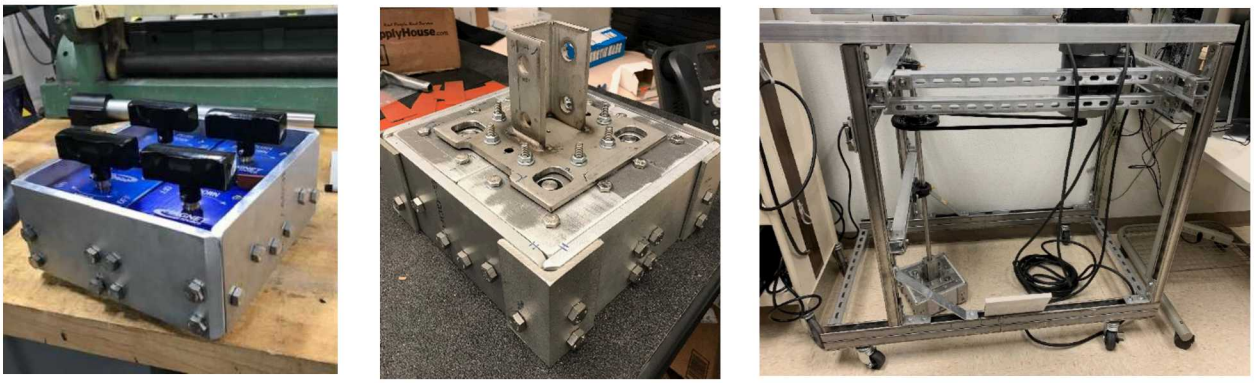

Figure 21: Left: Magnets being placed into the rotating stage mount. Center: Assembly of the drive shaft mount. Right: Full prototype variable speed rotating magnetic state assembly.

For initial field tests, the rotating stage prototype was moved outside for preliminary measurements. Figure 22 shows a drawing of how a full mobile device might look; for this phase we simply used the electronics cart we have assembled in the lab and wheeled it out together with the magnet stage without an attempt to consolidate the two. In practice, one unit comprised of the two would be much more convenient.

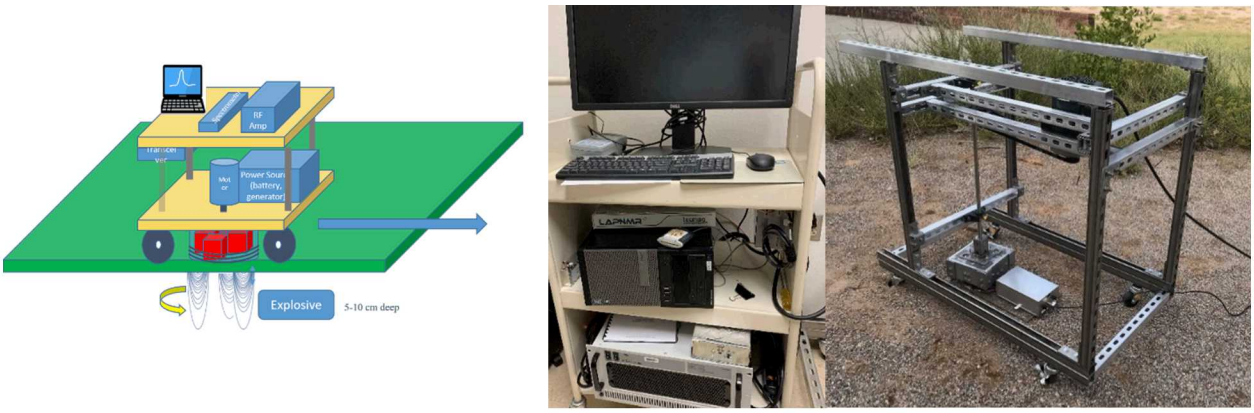

Figure 22: Left: Consolidated electronics and rotating magnet stage concept. Right: electronics cart and rotating magnet stage prototype in the field.

Initial experiments using used the SLMP pulse sequence detailed in Section 5.3 for the acquisition sequence. The magnet state was rotated at ~15 Hz such that the center of one of the magnets moved from maximum field to minimum field (approximately $\frac{\pi}{4}$ radians) in approximately 10 ms, the cross-polarization mixing time of the two transitions.[30] Our best attempts so far have resulted in an SNR enhancement of about a factor of 5 out of a theoretical enhancement of over 12 times for the same acquisition time. Clearly more optimization is required, but the proof-of-principle is shown to be effective.

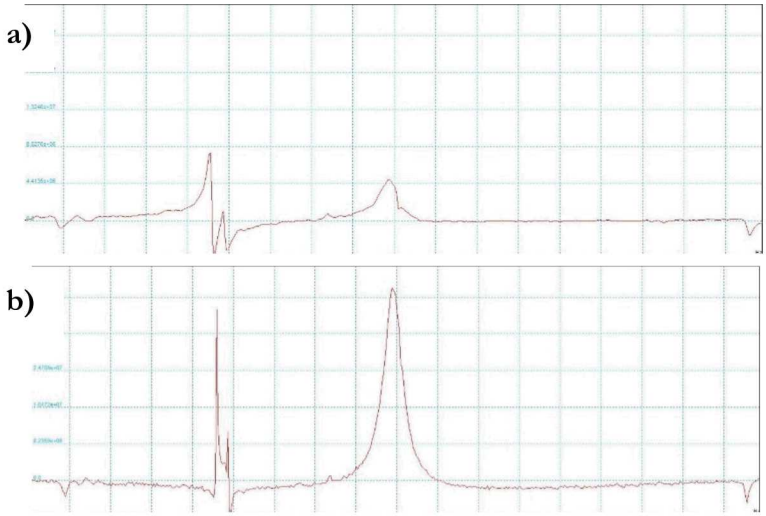

Figure 23: ^{14}N NQR signals acquired using the SLMP pulse sequence. a) Signal acquired with magnets turned off (but stage spinning). b) signal acquired with magnets turned on and stage spinning.

The apparent signals at lower frequency (left) of the main peak and at the far right are noise and are present with the motor not running. These spurious peaks, as well as the overall noise level, motivate the need to consider RFI mitigation techniques.

4.5. RFI mitigation

In a laboratory setting, it is straightforward to shield a measurement from RF noise, but it can be more difficult in a field environment. Mitigating RF noise can be a bit of an art as well, with many people disagreeing about best practices. For example, Garroway found that gradiometer coils (such as a figure-eight coil or axial gradiometer) can reduce far field noise by as much as 30 dB,[2] while Ostafin notes that gradiometers aren't a good choice due to the reduced inductance they cause and advocates instead for additional antennas with active subtraction.[14] The active approach was pursued by Quantum Magnetics, employing an efficient NQR coil and an external remote antenna to pick up and subtract RF interference. For this approach to work, high dynamic range and careful balancing are required.

It is worth emphasizing that NQR detectors are limited by their own random thermal noise, as opposed to systematic noise of clutter, background, soil, etc. This is important because such a device can clear its own errors by simply averaging longer. For example, it might advantageous to use the NQR device in sweep mode and clear any errors by trading off improved SNR for averaging time by sitting in once place and averaging longer.

5. NQR AS A NON-DESTRUCTIVE TEST PLATFORM

5.1. Polymer Stress

Thermoset polymers are used throughout Sandia's mission space. In many applications, stress induced by the curing process can cause damage to other components, and reliable measures of that stress are important. NQR can provide useful information in studying the thermal and elastic properties of polymers since it is sensitive to minute changes in pressure and temperature of samples.[31] Moreover, use of a surface coil and gradients has been shown to be able to perform contactless stress imaging for rubber-like matrices.[32] Crystals and epoxy resins are also amenable to NQR investigations, but the resonance lines are considerably broader.

To partially mitigate the lack of order in some polymer matrices, one can dope the polymer pre-cure with an NQR-active tracer particle such as Cu_2O. Such a tracer needs to meet the following criteria:

1. It should be well-detectable in small amounts
2. It should have a linearly pressure dependent resonance at constant temperature
3. It should be chemically inert in the epoxy matrix

When these criteria are met, the tracer particle can act as a crystalline stress detector in the matrix. As the polymer is stressed, the dopant particles are also stressed and shifts in the NQR frequency are observed. A shift in the NQR resonance is proportional to the mean value of the internal stress, while the line broadening is a measure of the deviation of the local pressure from its mean value.[32] Use of tracer particles in polymers to measure stress and temperature have been performed by a number of groups.[31,33-35]

5.1.1. Experiments

We performed some preliminary experiments to determine the feasibility of using NQR for aging and stress determinations. First, Epon 828 resin (difunctional bisphenol A/epichlorohydrin derived liquid epoxy resin) was mixed with 5%, 10%, and 15% Cu_2O particles by volume and cured with isophorone diamine (IPDA). The samples were then introduced into the NQR probe and placed in a temperature-controlled oven. Spectra were recorded as a function of temperature from room temperature to 330 °C. Figure 24 shows the frequency shift of the ^{63}Cu NQR resonance as function of temperature in both the epoxy-encased sample and a bare Cu_2O sample. The bare Cu_2O signal shows a temperature response of 3.6819 kHz/K, while the epoxy/Cu_2O system showed a 3.7388 kHz/K response. Therefore, the strain component is 3.7388-3.6819 = 0.0569 kHz/K. This suggests the path forward for these types of measurements: using the coefficient of thermal expansion (CTE) for these materials, the ratio of that 0.0569 kHz/K figure and the CTE (in %/K) should give us a figure for strain response (kHz/%). This can then be verified against temperature-corrected tensile test data and one can also back out the polymer shrinkage. The epoxy samples with different Cu_2O content have almost identical frequencies and temperature dependence (3.7388, 3.7362, and 3.7328 kHz/K at 15, 10, and 5% Cu_2O, respectively). While the effect of temperature dominates, the effect of strain is clearly embedded in these data.

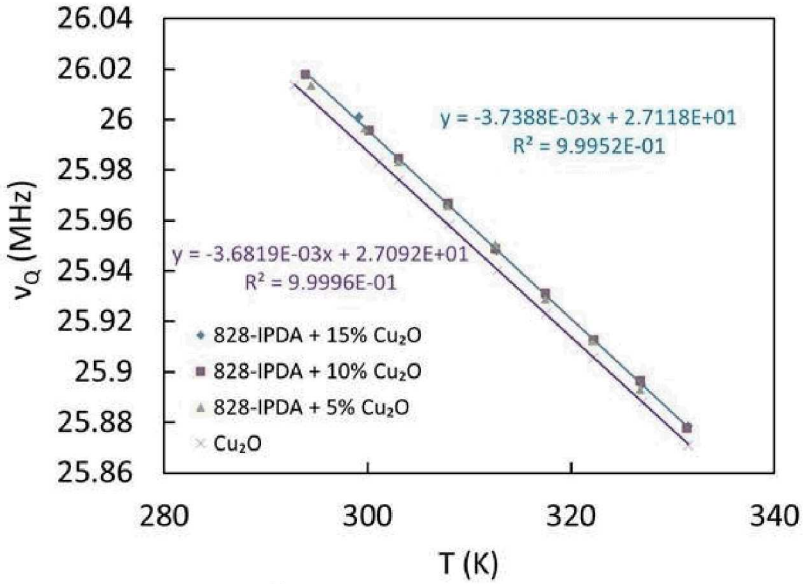

Figure 24: Temperature response of the ^{63}Cu NQR frequency on an epoxy-encased polymer and a bare Cu_2O sample.

One caveat in preparing these samples is that the tracer particles (Cu_2O in our case) can become inhomogeneously distributed during the curing process as the tracer particles settle out due to gravity. Figure 25 shows optical images of some of our early attempts, showing the discontinuity between the tracer-rich phase and tracer-poor phase created by this settling. Subsequent attempts corrected this problem by rotating the mold during the curing process.

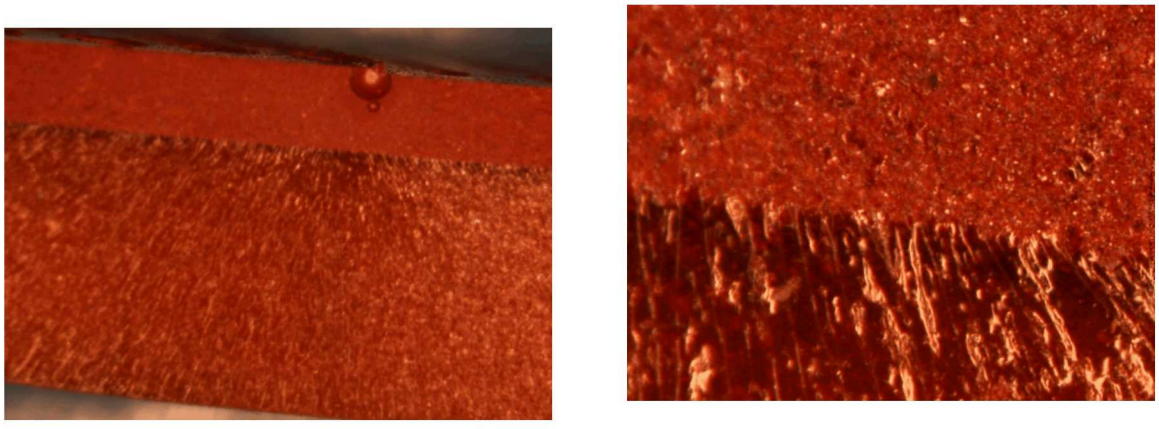

Figure 25: Optical images of cured epoxy/Cu_2O showing the inhomogeneous mixing of the tracer particles due to settling.

Once homogeneous mixtures were obtained and the temperature responses of the mixtures we built a custom NQR probe that tunes to the ^{63}Cu NQR resonance at 26 MHz and allows the

to pass through the probe body for loading with a load frame. The probe and physical setup of the experiment is shown in

Figure 26.

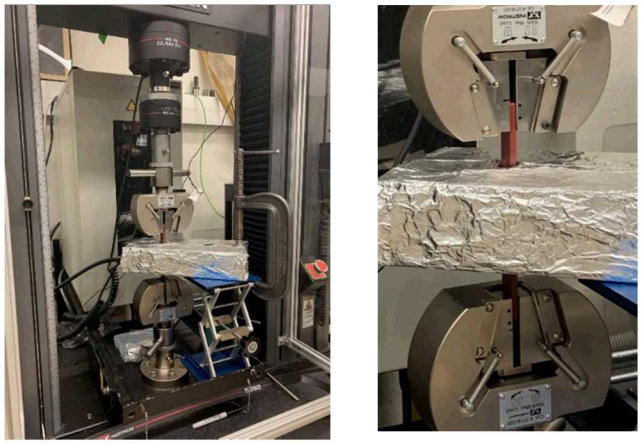

Figure 26: Experimental setup for polymer stress experiments. Left: sample and probe in the load frame. Right: Close up of the probe and sample in the load frame jaws.

An NQR probe was constructed that allows the sample (~15 cm x 2 cm) to pass through the probe via the inductor so that both ends can be clamped into the load frame jaws. In this configuration, constant stress can be applied to the sample with the mechanical strain measured separately.

Figure 27 shows the results of the stress/strain experiments at constant temperature. On the left panel, the superimposed spectra are shown from 0 to 0.6% strain. Each peak can be well approximated by a Gaussian and the peak position extracted. The position of the peak as a function of the polymer strain

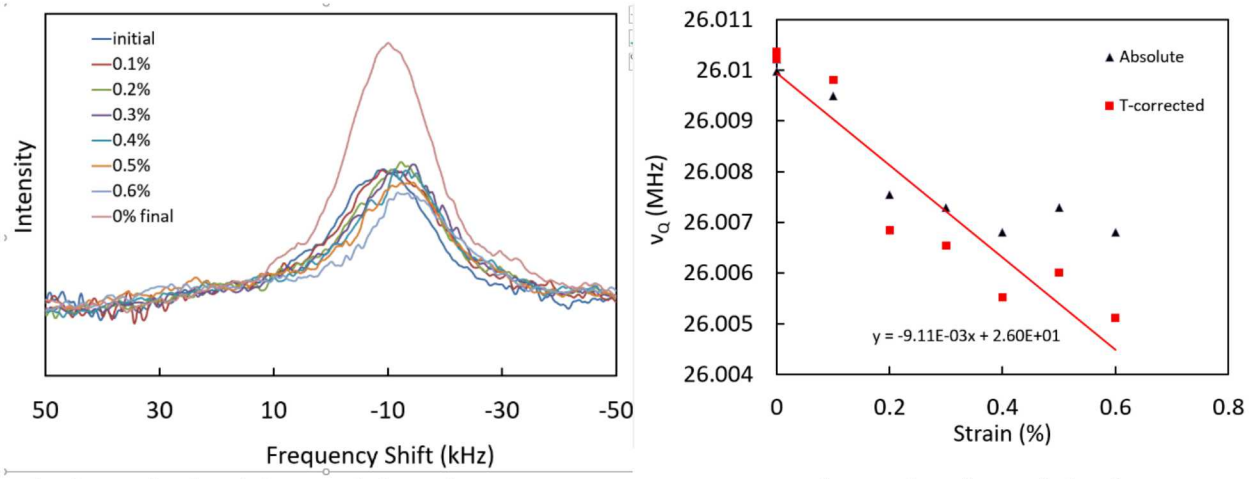

is shown in the right panel. Sample temperatures were measured at each point and the data corrected for temperature.

Figure 27: ^{63}Cu NQR of the 828-IPDA epoxy/Cu_2O system at 10 vol% tracer particle loading. Left: Lineshapes of the ^{63}Cu resonance as a function of strain. Right: Absolute (triangles) and temperature-corrected (squares) frequency shifts as a function of polymer strain.

Figure 27 shows a clear frequency shift response for the homogenous component of stress applied to the sample, as well as a broadening associated with inhomogeneous stress. It is worth noting that the applied stress is uniaxial in the case of the load frame. This is a somewhat different case than that of the isotropic expansion shown in Figure 24. Isotropic expansion/contraction of the polymer matrix leads to isotropic expansion/contraction of the embedded Cu_2O. The NQR response due to polymer expansion/contraction estimated from those experiments was -11 kHz/%. However, it seems reasonable that that this is not the NQR strain response of pure Cu_2O. The modulus of Cu_2O is 1-2 orders of magnitude greater than the polymer matrix. Therefore, the strain in the Cu_2O is going to be considerably less than the strain in the polymer. In other words, the NQR strain response of pure Cu_2O should be significantly higher in magnitude than -11 kHz/%.

The situation becomes even less clear in uniaxial tension. Assuming an isotropic initial distribution of quadrupolar moments in the specimen in terms of orientation, those moments more closely aligned with the deformation axis will experience tension, while those more closely aligned with the perpendicular axes will experience compression. The magnitude of compression in those perpendicular axes is reduced by Poisson's ratio. All these forces will also be scaled by the difference in modulus, as mentioned above. A finite element model could tease out the strain distribution based on material properties of the individual components. Nonetheless, these initial results demonstrate that the peak of the frequency response does shift and broaden with overall tensile strain. The peak frequency should also decrease with overall tensile strain (essentially because Poisson's ratio for a glassy polymer is 0.3-0.4), but the NQR strain response in this scenario should be different from the CTE isotropic expansion scenario.

5.1.2. Simulations

In order to better understand the strain data in Figure 27, density function theory (DFT) and *ab initio* molecular dynamics (AIMD) simulation were performed on the Cu_2O lattice. Crystal structures were imported from the Crystallography Open Database (COD),[36] and structural relaxation was performed using periodic density functional theory (DFT) calculations with the Quantum Espresso [37] open source electronic structure code. Norm-conserving pseudopotentials[38] with the generalized gradient approximation in the form of Perdew, Burke, and Ernzerhof (PBE)[39] were implemented. An energy cut-off of 160 Ry and a 5x5x5 k-point matrix were used. The structure model consists of four Cu atoms and two O atoms with a cubic crystal structure and a $Pn\bar{3}m$. To monitor the impact of temperature on the NQR spectra two types of calculations were performed, one static and one dynamic. For the static condition, the lattice of the Cu_2O structure was expanded in increments of 0.1Å either anisotropically or isotopically and the NQR was calculated. This assumes that all the impact of the temperature is a result of lattice expansion and does not include dynamic changes in the atomic positions as a function of elevated temperature. For the dynamic condition AIMD simulations were performed at four different temperatures (T = 300 K, 310 K, 320 K, and 330 K) that mimic the experimental conditions studied. Using AIMD includes the density of the Cu_2O evolves as a function of temperature, as does the NQR values for Cu and O nuclei. Default time steps were used of 20.0 a.m.u. (0.48 fs). Dispersion corrections were not included in the simulations. A total of 7500 time

steps were run at each of the four temperatures, and the average of the last 2500 steps are reported with the average and standard deviation. Using only the last portion of the trajectory removes variation from the initial structural relaxation (see Figure 30). The ^{63}Cu and ^{17}O NQR was calculated from the relaxed Cu_2O structure either after anisotropic or isotropic stretching of the unit cell, or at each step along the AIMD trajectory using the GIPAW (Gauge Including Projector Augmented Waves) model.[40-42]

Cu_2O has been extensively studied using DFT methods due to its unique properties including a negative coefficient of thermal expansion below 200 K.[43-45] The lattice parameter of the Cu_2O structure model in this work is 4.43 Å at 300 K, within the range of 4.22-4.46 Å that has been reported by previous computational investigations[46-48] and is within 0.15 Å of the experimentally reported values.[44,49,50] In addition to comparing the lattice parameter, the coefficient of thermal expansion (CTE) also needs to be accurately represented by the Cu_2O structure model. Here, the change in volume with temperature results in a CTE in the range of 5-6 10^{-6} K^{-1} depending on how the CTE is calculated. A plot of the average change in volume and the average change in temperature along the AIMD trajectories is included in Figure 31. This value is comparable with the value reported by $1.9x10^{-6}$ K^{-1} [51]. Therefore, there can be confidence that the response of the Cu_2O unit cell to temperature is well represented by the computational results and can be used in further analysis.

To evaluate the hypothesis that changes in the NQR spectra of polymers containing Cu_2O tracer particles is a result of the expansion of the Cu_2O unit cell, the first step was a static calculation. Controlled expansion of the unit cell results in a significant decrease in the ^{63}Cu NQR shift (Figure 28a). Interestingly, the expansion of the unit cell isotopically vs. anisotropically did not appear to generate differences, and it is the bulk change in the Cu-O distance that is resulting in the NQR shift. The differences in the NQR tracks linearly with the expansion of the Cu-O bond (see Figure 28b.)

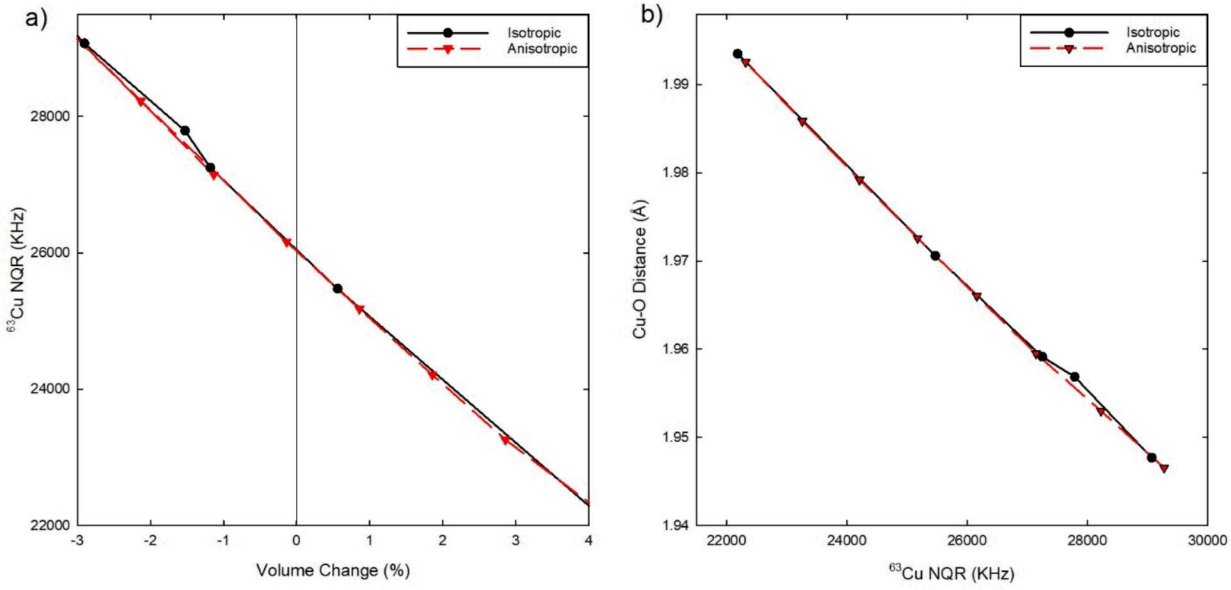

Figure 28: (a) change in ^{63}Cu NQR spectra with volume change of the unit cell and (b) the Cu-O distance (Å)

From the AIMD trajectories, variability in the atomic position and cell volume as a function of temperature can be included in the trend of ^{63}Cu NQR as a function of temperature. Experimental data found that the ^{63}Cu NQR varies by -3.68 kHz/K with temperature (see Section 5.1.1). Given that ^{63}Cu NQR values are commonly reported as MHz, a slope of -3.7x10^{-6} MHz/K is a relatively subtle change in slope to be captured by computational methods. The data here results in similarly subtle changes of the ^{63}Cu NQR values as a function of temperature. When only the last 2500 steps of the simulation are used, and the Cu_2O structure is the most relaxed, the slope is 1.7 kHz/K. When the entire AIMD trajectory is considered the slope of ^{63}Cu NQR with temperature is -8.00 kHz/K. See the plots of the ^{63}Cu NQR data with temperature in Figure 29. To facilitate visualization of the data the error bars are the standard error, rather than the standard deviation. The computational results are of the same order of magnitude as the experimental results, and overall indicate the same trend. It is recommended that longer simulations (of 10+ ps of simulation time) and at higher temperature (340 K, 350 K) are performed to further confirm the trend.

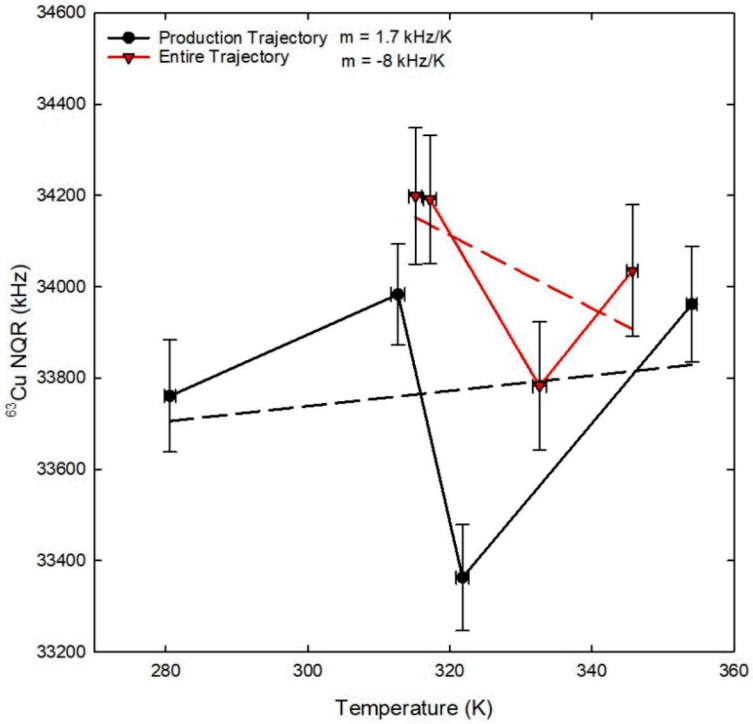

Figure 29: Trend of ^{63}Cu NQR (kHz) and temperature (K) for two different portions of the AIMD trajectory (i) the production trajectory, the last 2500 steps and (ii) the entire AIMD trajectory. Error bars are the standard error and linear regressions are included as dotted lines. The slope of the linear regression is reported in kHz/K.

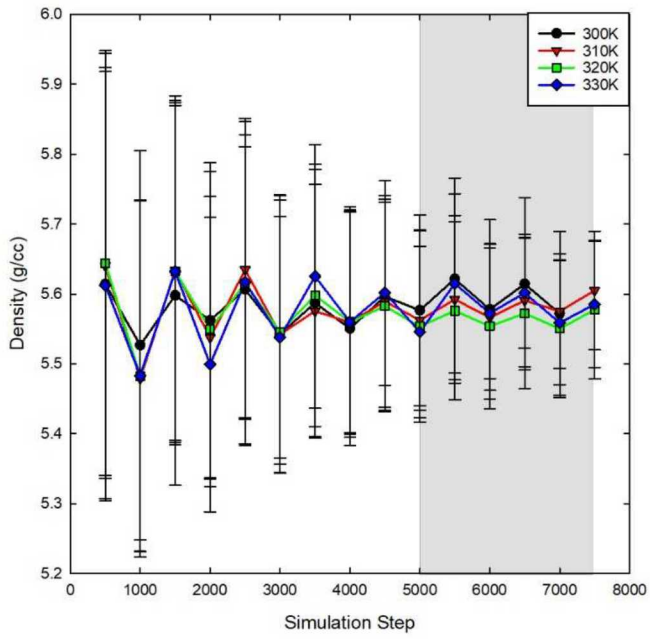

Figure 30. Change in density along the AIMD trajectories with four different target temperatures (300 K, 310 K, 320 K, 330 K). The region shaded in grey is the portion of the AIMD trajectory that is used for analysis.

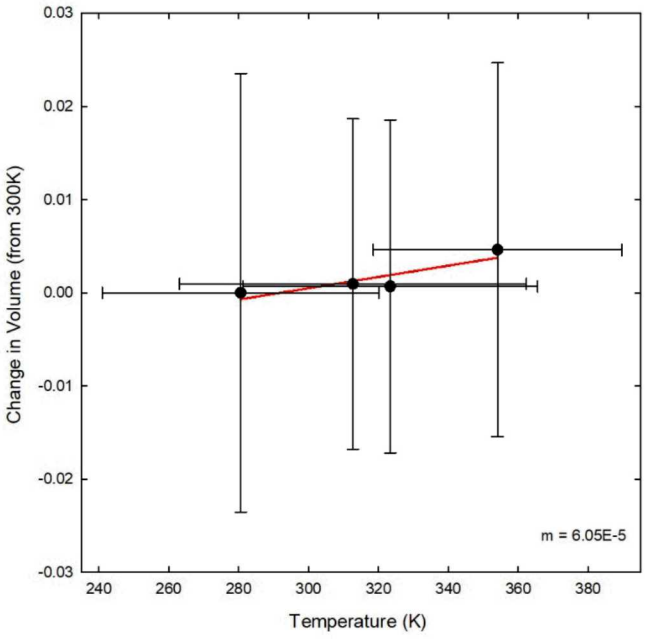

Figure 31. Change in volume and temperature of AIMD trajectories from the last 2500 steps of the simulation. The red line is a linear regression (with m = 6.05×10^{-5} and R^2=0.78) to calculate the coefficient of thermal expansion (CTE).

5.2. Future Directions

Based on the initial success of the polymer strain experiments, the Lifetime and Ageing program based out of 1800 has agreed to continue to investigate the use of NQR as an NDT tool for possible use in surveillance. Components of interest that we will explore going forward include lightning arrestor connectors, foam encapsulants, glass-metal seals, carbon fiber matrices, flat flex cabling, and corrosion in additional components.

Another potential application for NQR as a standoff detector is in opioid detection in the mail and other small packages. Several groups have applied NQR to this purpose.[3,28,52,53] Detection schemes applied to the US mail are manual and cursory; a rapid and effective screening technique that could non-invasively identify illicit compounds in the mail stream would be quite useful.

6. CONCLUSIONS

NQR for explosive detection has enjoyed many years of development. However, SNR enhancement techniques that include spin-lock pulse sequences and double resonance techniques have not found wide application in field situations. Recent advances in NMR/NQR transmit/receive electronics have made application of those techniques more feasible. In addition, the time-varying rotating magnet stage innovated in this work helps make cross-polarization from ^{1}H to ^{14}N in the field more robust and useful. We have been able to speed to SNR/time of field acquisitions by implementing these enhancement techniques.

The lab based NQR capability as an NDT is now established, and preliminary data were obtained on a polymer/tracer system to measure the strain in a cured epoxy. Based on the success of that work, we anticipate broadening the application space for NDT NQR work within the Ageing programs at Sandia to look at other components.

REFERENCES

(1) Buess, M.; Garroway, A.; Miller, J. NQR detection using a meanderline surface coil. *Journal of Magnetic Resonance (1969)* **1991,** *92* (2), 348.

(2) Garroway, A. N.; Buess, M. L.; Miller, J. B.; Suits, B. H.; Hibbs, A. D.; Barrall, G. A.; Matthews, R.; Burnett, L. J. Remote sensing by nuclear quadrupole resonance. *IEEE Transactions on Geoscience and Remote Sensing* **2001,** *39* (6), 1108.

(3) Yesinowski, J. P.; Buess, M. L.; Garroway, A. N.; Ziegeweid, M.; Pines, A. Detection of 14N and 35Cl in cocaine base and hydrochloride using NQR, NMR, and SQUID techniques. *Anal. Chem.* **1995,** *67* (13), 2256.

(4) Suits, B.; Garroway, A.; Miller, J. Super-QDetection of Transient Magnetic Resonance Signals. *J. Magn. Reson.* **1998,** *132* (1), 54.

(5) Hibbs, A. D.; Barrall, G. A.; Beevor, S.; Burnett, L. J.; Derby, K.; Drew, A.; Gregory, D. M.; Hawkins, C.; Huo, S.; Karunaratne, A. Detection and Remediation Technologies for Mines and Minelike Targets V, 2000; p 564.

(6) Hibbs, A. D.; Barrall, G. A.; Czipott, P. V.; Lathrop, D. K.; Lee, Y.; Magnuson, E. E.; Matthews, R.; Vierkotter, S. A. Detection and Remediation Technologies for Mines and Minelike Targets III, 1998; p 522.

(7) Kim, Y.; Karaulanov, T.; Matlashov, A.; Newman, S.; Urbaitis, A.; Volegov, P.; Yoder, J.; Espy, M. Polarization enhancement technique for nuclear quadrupole resonance detection. *Solid State Nucl. Magn. Reson.* **2014,** *61*, 35.

(8) Malone, M.; McGillvray, M.; Sauer, K. Revealing dipolar coupling with NQR off-resonant pulsed spin locking. *Phys. Rev. B* **2011,** *84* (21), 214430.

(9) Miller, J. B.; Barrall, G. A. Explosives detection with nuclear quadrupole resonance: an emerging technology will help to uncover land mines and terrorist bombs. *American scientist* **2005,** *93* (1), 50.

(10) Cooper, R. J.; Prescott, D. W.; Matz, P.; Sauer, K. L.; Dural, N.; Romalis, M. V.; Foley, E. L.; Kornack, T. W.; Monti, M.; Okamitsu, J. Atomic magnetometer multisensor array for rf interference mitigation and unshielded detection of nuclear quadrupole resonance. *Physical Review Applied* **2016,** *6* (6), 064014.

(11) Thurber, K. R.; Sauer, K. L.; Buess, M. L.; Klug, C. A.; Miller, J. B. Increasing 14N NQR signal by 1H–14N level crossing with small magnetic fields. *J. Magn. Reson.* **2005,** *177* (1), 118.

(12) Smith, J. A. Nuclear quadrupole resonance spectroscopy. General principles. *J. Chem. Educ.* **1971,** *48* (1), 39.

(13) Suits, B. H. In *Handbook of Applied Solid State Spectroscopy*; Springer, 2006.

(14) Ostafin, M.; Nogaj, B. 14N-NQR based device for detection of explosives in landmines. *Measurement* **2007,** *40* (1), 43.

(15) Oja, T.; Marino, R.; Bray, P. 14N nuclear quadrupole resonance in the ferroelectric phase of sodium nitrite. *Phys. Lett. A* **1967,** *26* (1), 11.

(16) Petersen, G.; Bray, P. 14N nuclear quadrupole resonance and relaxation measurements of sodium nitrite. *J. Chem. Phys.* **1976,** *64* (2), 522.

(17) Itozaki, H. In *Anti-personnel Landmine Detection for Humanitarian Demining*; Springer, 2009.

(18) Seliger, J.; Žagar, V.; Blinc, R. 14 N NQR study of the structural phase transitions in NH 4 NO 3. *Zeitschrift für Physik B Condensed Matter* **1989,** *77* (3), 439.

(19) Rudakov, T. Some aspects of the effective detection of ammonium nitrate-based explosives by pulsed NQR method. *Appl. Magn. Reson.* **2012,** *43* (4), 557.

(20) Cardona, L.; Miyato, Y.; Itozaki, H.; Jiménez, J.; Vanegas, N.; Sato-Akaba, H. Remote detection of ammonium nitrate by nuclear quadrupole resonance using a portable system. *Appl. Magn. Reson.* **2015,** *46* (3), 295.
(21) Marino, R.; Klainer, S. Multiple spin echoes in pure quadrupole resonance. *J. Chem. Phys.* **1977,** *67* (7), 3388.
(22) Ostroff, E.; Waugh, J. Multiple spin echoes and spin locking in solids. *Phys. Rev. Lett.* **1966,** *16* (24), 1097.
(23) Mansfield, P.; Ware, D. Nuclear resonance line narrowing in solids by repeated short pulse rf irradiation. *Phys. Lett.* **1966,** *22* (2), 133.
(24) Suwelack, D.; Waugh, J. Quasistationary magnetization in pulsed spin-locking experiments in dipolar solids. *Phys. Rev. B* **1980,** *22* (11), 5110.
(25) Rudakov, T.; Mikhaltsevich, V. Multiple NQR spin echoes in phase cycled pulse experiments. *Phys. Lett. A* **2003,** *309* (5-6), 465.
(26) Mozzhukhin, G. V.; Rameev, B. Z.; Kupriyanova, G. S.; Aktaş, B. In *Magnetic Resonance Detection of Explosives and Illicit Materials*; Springer, 2014.
(27) Luznik, J.; Pirnat, J.; Trontelj, Z. Polarization enhanced 14N NQR detection with a nonhomogeneous magnetic field. *Solid State Commun.* **2002,** *121* (12), 653.
(28) Blinc, R.; Seliger, J.; Zidans, A.; Žagar, V.; Milia, F.; Robert, H. 14N nuclear quadrupole resonance of some sulfa drugs. *Solid State Nucl. Magn. Reson.* **2006,** *30* (2), 61.
(29) Riggin, M.; Knispel, R.; Pintar, M. Cation diffusion study in NH4NO3 by proton spin relaxation. *J. Chem. Phys.* **1972,** *56* (6), 2911.
(30) Prescott, D.; Olmedo, O.; Soon, S.; Sauer, K. Low-field approach to double resonance in nuclear quadrupole resonance of spin-1 nuclei. *J. Chem. Phys.* **2007,** *126* (20), 204504.
(31) Ainbinder, N.; Azheganov, A.; Danilov, A.; Shestakova, N. Application of the NQR method for studying polymer materials. *J. Mol. Struct.* **1995,** *345*, 105.
(32) Nickel, P.; Robert, H.; Kimmich, R.; Pusiol, D. NQR method for stress and pressure imaging. *J. Magn. Reson., Ser A* **1994,** *111* (2), 191.
(33) Hewitt, R.; Mazelsky, B. Nuclear quadrupole resonance as a nondestructive probe in polymers. *J. Appl. Phys.* **1972,** *43* (8), 3386.
(34) Tarasov, V. P.; Erofeeve, L. N.; Dzhavadyan, E. A.; Smirnov, Y. N.; Rozenburg, B. A. Pulsed NQR for Measuring Internal Stresses in Polymers and Composites. *Heterophase Network Polymers: Synthesis, Characterization, and Properties* **2019**, 301.
(35) Vierkoetter, S. A.; Ward, C. R.; Gregory, D. M.; Menon, S. M.; Roach, D. P. Nondestructive Evaluation and Health Monitoring of Aerospace Materials and Composites II, 2003; p 176.
(36) Gražulis, S.; Chateigner, D.; Downs, R. T.; Yokochi, A.; Quirós, M.; Lutterotti, L.; Manakova, E.; Butkus, J.; Moeck, P.; Le Bail, A. Crystallography Open Database–an open-access collection of crystal structures. *J. Appl. Crystallogr.* **2009,** *42* (4), 726.
(37) Giannozzi, P.; Baroni, S.; Bonini, N.; Calandra, M.; Car, R.; Cavazzoni, C.; Ceresoli, D.; Chiarotti, G. L.; Cococcioni, M.; Dabo, I. QUANTUM ESPRESSO: a modular and open-source software project for quantum simulations of materials. *J. Phys.: Condens. Matter* **2009,** *21* (39), 395502.
(38) Kresse, G.; Hafner, J. Norm-conserving and ultrasoft pseudopotentials for first-row and transition elements. *J. Phys.: Condens. Matter* **1994,** *6* (40), 8245.
(39) Perdew, J. P.; Burke, K.; Ernzerhof, M. Generalized gradient approximation made simple. *Phys. Rev. Lett.* **1996,** *77* (18), 3865.
(40) Pickard, C. J.; Mauri, F. All-electron magnetic response with pseudopotentials: NMR chemical shifts. *Phys. Rev. B* **2001,** *63* (24), 245101.

(41) Harris, R. K.; Hodgkinson, P.; Pickard, C. J.; Yates, J. R.; Zorin, V. Chemical shift computations on a crystallographic basis: some reflections and comments. *Magn. Reson. Chem.* **2007,** *45* (S1), S174.
(42) Charpentier, T. The PAW/GIPAW approach for computing NMR parameters: A new dimension added to NMR study of solids. *Solid State Nucl. Magn. Reson.* **2011,** *40* (1), 1.
(43) Gupta, M.; Mittal, R.; Chaplot, S.; Rols, S. Phonons, nature of bonding, and their relation to anomalous thermal expansion behavior of M2O (M= Au, Ag, Cu). *J. Appl. Phys.* **2014,** *115* (9), 093507.
(44) Sanson, A.; Rocca, F.; Dalba, G.; Fornasini, P.; Grisenti, R.; Dapiaggi, M.; Artioli, G. Negative thermal expansion and local dynamics in Cu 2 O and Ag 2 O. *Phys. Rev. B* **2006,** *73* (21), 214305.
(45) White, G. Thermal expansion of cuprous oxide at low temperatures. *Journal of Physics C: Solid State Physics* **1978,** *11* (11), 2171.
(46) Cortona, P.; Mebarki, M. Cu2O behavior under pressure: an ab initio study. *J. Phys.: Condens. Matter* **2011,** *23* (4), 045502.
(47) Soon, A.; Todorova, M.; Delley, B.; Stampfl, C. Thermodynamic stability and structure of copper oxide surfaces: A first-principles investigation. *Phys. Rev. B* **2007,** *75* (12), 125420.
(48) Ruiz, E.; Alvarez, S.; Alemany, P.; Evarestov, R. A. Electronic structure and properties of Cu 2 O. *Phys. Rev. B* **1997,** *56* (12), 7189.
(49) Beg, M.; Shapiro, S. Study of phonon dispersion relations in cuprous oxide by inelastic neutron scattering. *Phys. Rev. B* **1976,** *13* (4), 1728.
(50) Hallberg, J.; Hanson, R. The elastic constants of cuprous oxide. *physica status solidi (b)* **1970,** *42* (1), 305.
(51) Reimanis, I. E.; Trumble, K. P.; Rogers, K. A.; Dalgleish, B. J. Influence of Cu2O and CuAlO2 Interphases on Crack Propagation at Cu/α□Al2O3 Interfaces. *J. Am. Ceram. Soc.* **1997,** *80* (2), 424.
(52) Blinc, R.; Apih, T.; Seliger, J. Nuclear quadrupole double resonance techniques for the detection of explosives and drugs. *Appl. Magn. Reson.* **2004,** *25* (3-4), 523.
(53) Slusher, R.; Hahn, E. Sensitive detection of nuclear quadrupole interactions in solids. *Phys. Rev.* **1968,** *166* (2), 332.

DISTRIBUTION

Email—Internal

Name	Org.	Sandia Email Address
Technical Library	01977	sanddocs@sandia.gov

Email—External (encrypt for OUO)

Name	Company Email Address	Company Name

Hardcopy—Internal

Number of Copies	Name	Org.	Mailstop

Hardcopy—External

Number of Copies	Name	Company Name and Company Mailing Address

This page left blank

This page left blank

Sandia National Laboratories

Sandia National Laboratories is a multimission laboratory managed and operated by National Technology & Engineering Solutions of Sandia LLC, a wholly owned subsidiary of Honeywell International Inc. for the U.S. Department of Energy's National Nuclear Security Administration under contract DE-NA0003525.